NEWTONIAN AND VISCOELASTIC LIQUID JET IMPINGEMENT ON A MOVING SURFACE

by

Yuchen Guo

B.E., Nanjing University of Aeronautics and Astronautics, 2011

A THESIS SUBMITTED IN PARTIAL FULFILLMENT OF

THE REQUIREMENTS FOR THE DEGREE OF

MASTER OF APPLIED SCIENCE

in

THE FACULTY OF GRADUATE AND POSTDOCTORAL STUDIES

(Mechanical Engineering)

THE UNIVERSITY OF BRITISH COLUMBIA

(Vancouver)

November 2014

Abstract

Motivated by the need to improve transfer efficiencies of liquid coatings from jet impingement in railroad friction control applications, an experimental investigation into Newtonian and viscoelastic liquid jet impingement on moving surfaces is presented.

Seven PEO-glycerine-water solutions and three commercial liquid friction modifiers were tested with a variety of jet speeds, jet diameters, surface speeds and surface roughnesses. The effects of these test conditions on jet impingement splash behaviours as well as jet and lamella geometries were studied. High-speed imaging was employed to visualize the interaction between the impinging jet and the moving surface.

Experiments on the effect of modest surface roughness revealed that, while jet and surface speed were both important factors, splash was more likely to occur on surfaces with lower roughness levels. By analyzing experimental results for Newtonian liquids, a relation between lamella geometry and test conditions were found, which can be used to predict lamella dimensions. Three types of non-Newtonian behaviours were observed at high surface speed and low jet speed: jet necking, jet bending and jet stretching.

Preface

The authors of Chapter 2 are Yuchen Guo and Dr. Sheldon Green. Dr. Green identified the need to experimentally study the impingement behaviour of Newtonian and viscoelastic liquid jet on a moving surface. I put together the experimental set-ups under the supervision of Dr. Green and the UBC safety committee. I wrote the manuscript with the revisions and suggestions from Dr. Green.

A version of Chapter 2 has been submitted for publication: Guo,Y. and Green,S.I. "Experimental Methods for Examining High Speed Liquid Jet Impaction on a Moving Surface", 2014.

The authors of Chapter 3 are Yuchen Guo and Dr. Sheldon Green. Dr. Green identified the need to further the understanding of the impingement behaviour of Newtonian and viscoelastic liquid jet on a moving surface. I conducted the experiments and performed the data analysis with directions from Dr. Green. I wrote the manuscript with the revisions and suggestions from Dr. Green.

Table of Contents

Abstract ..... **ii**

Preface ..... **iii**

Table of Contents ..... **iv**

List of Tables ..... **viii**

List of Figures ..... **ix**

List of Equations ..... **xiii**

Glossary ..... **xiv**

Acknowledgements ..... **xvi**

Chapter 1: Introduction **1**

1.1 Motivation 1

1.1.1 Friction control in railroad industry 1

1.1.2 Liquid friction modifier (LFM) and application methods 2

1.2 Liquid jet impingement 3

1.2.1 Impingement on a stationary surface 3

1.2.2 Impingement on moving surface 4

1.3 Research objectives 6

Chapter 2: Methodology **8**

2.1 Test liquids construction and characterization 8

2.1.1 Solution preparation 8

2.1.2 Test liquid characterization 9

2.2 Flow rate test methods 12

2.2.1 Mass flow rate measurement 12
2.2.2 Liquid jet diameter measurement 13
2.3 Lab experiment method 13
2.4 Experimental apparatus for low speed impingement tests 15
2.4.1 Air cannon set-up 15
2.4.2 Impingement surfaces and wooden carrier (projectile) 17
2.4.3 Spray system 19
2.4.4 High-speed imaging system 20
2.4.5 Electrical control system 21
2.4.6 Safety considerations 22
2.5 Experimental apparatus for high speed impingement tests 23
2.5.1 Spinning disk set-up 23
2.5.2 High-speed imaging system 24
2.5.3 Safety considerations and electrical control system 25
Chapter 3: Results 26
3.1 Liquid jet properties 26
3.1.1 Flow rate test results 26
3.1.2 Liquid jet diameter measurements 30
3.2 Effects of surface roughness on liquid jet impingement 31
3.2.1 Commercial LFMs 31
3.2.2 Newtonian liquids 37
3.2.3 Effects of surface roughness summary 41
3.2.4 Splash triggered by jet or surface imperfection 41

3.3 High speed commercial LFMs jet impingement test results 43
3.4 Jet and lamella dimensions 44
3.4.1 Newtonian liquids 44
3.4.1.1 Lamella dimensions of interest 45
3.4.1.2 Lamella spread width and radius measurements 45
3.4.2 Non-Newtonian liquids 47
3.4.2.1 AP2 47
3.4.2.2 Simu 51
3.4.2.3 PEO-glycerine-water solutions 53
Chapter 4: Analysis and Discussion 54
4.1 Lamella dimensions for Newtonian liquids 54
4.1.1 Average lamella thickness *h* 54
4.1.1.1 Average lamella thickness theory 54
4.1.1.2 Effects of jet speed and surface speed 55
4.1.1.3 Effects of liquid viscosity 57
4.1.1.4 Effects of liquid jet diameter 59
4.1.2 Lamella shape ratio W/R 60
4.1.3 Newtonian liquids lamella dimensions summary 60
4.1.4 Newtonian liquids lamella dimensional analysis 63
4.1.5 Newtonian liquids lamella dimensions theory 66
4.2 Jet and lamella dimensions for non-Newtonian liquids 67
4.2.1 Lamella dimensions 67
4.2.2 Jet behaviours 68

Chapter 5: Conclusions and Recommendations 71

5.1 Conclusions for effect of surface roughness on splash characteristic..... 71

5.2 Conclusions for jet and lamella shape and dimensions 72

5.3 Recommendations for future work 73

Bibliography 74

List of Tables

Table 2-1 Compositions and properties of test liquids at 25°C 11

Table 2-2 Three stainless steel surfaces chosen to represent typical railroad track..... 18

Table 3-1 Empirical fit parameters: same nozzle, different liquids..... 28

Table 3-2 Empirical fit parameters: same test liquid, different nozzle sizes..... 29

Table 3-3 Nozzle diameter and liquid jet diameter measurement. 30

Table 3-4 Effects of surface roughness summary..... 41

List of Figures

Figure 1-1 Three distinct flow regimes. (a) Spatter (b) Deposition (c) Splash [24] 5

Figure 2-1 Phase separation due to PEO's low solubility in glycerine 9

Figure 2-2 Jet diameter measurement using imaging method. Nozzle diameter: 1854 μm. 13

Figure 2-3 Simplified boundary layer profiles. Lab environment (left) vs. field environment (right) 14

Figure 2-4 Schematic of air cannon test set-up for low speed impingement testing 16

Figure 2-5 Illustration of surface roughness measuring patterns 17

Figure 2-6 Measurements of surface roughness for nine different stainless steel plates 18

Figure 2-7 A wooden carrier (projectile) with three surfaces mounted on top used for low speed tests 19

Figure 2-8 Imaging set-up for recording high-speed videos with Phantom V611 camera 20

Figure 2-9 Electrical control system 21

Figure 2-10 Cross sectional views of projectile/barrel designs: 22

Figure 2-11 Schematic of spinning disk with two-camera imaging set-up illustration 23

Figure 2-12 High-speed imaging set-up for side view video recording 24

Figure 2-13 Photograph of the experiment apparatus used for high-speed tests 25

Figure 3-1 Model elastic and inelastic liquids mass flow rate test results. Nozzle orifice diameter: 648 μm. 27

Figure 3-2 Discharge coefficient for water-glycerine solutions as a function of Reynolds number 27

Figure 3-3 Mass flow rate test results: 85% aqueous glycerine solution, varying nozzle orifice diameters. 28
Figure 3-4 Mass flow rate test results for commercial LFMs. Nozzle orifice diameter: 648 μm. 29
Figure 3-5 AP2 liquid jet impingement on mirror surface test results 32
Figure 3-6 AP2 liquid jet impingement on smooth surface test results 32
Figure 3-7 AP2 liquid jet impingement on rough surface test results 33
Figure 3-8 45oC liquid jet impingement on mirror surface test results 34
Figure 3-9 45oC liquid jet impingement on smooth surface test results 34
Figure 3-10 45oC liquid jet impingement on rough surface test results 35
Figure 3-11 Simu liquid jet impingement on mirror surface test results 36
Figure 3-12 Simu liquid jet impingement on smooth surface test results 36
Figure 3-13 Simu liquid jet impingement on rough surface test results 37
Figure 3-14 GW70 liquid jet impingement on mirror surface test results 38
Figure 3-15 GW70 liquid jet impingement on smooth surface test results 38
Figure 3-16 GW70 liquid jet impingement on rough surface test results 39
Figure 3-17 GW85 liquid jet impingement on mirror surface test results 39
Figure 3-18 GW85 liquid jet impingement on smooth surface test results 40
Figure 3-19 GW85 liquid jet impingement on rough surface test results 40
Figure 3-20 Time sequence showing the transition from jet deposition to jet splash. In this sequence the transition is caused by very fine droplets adhering to the otherwise dry substrate. 42
Figure 3-21 Time sequence showing the transition from jet deposition to jet splash. In this sequence the transition is caused by a small air bubble in the jet that perturbs the flow. 42
Figure 3-22 Simu liquid jet high speed impingement test results 43

Figure 3-23 AP2 liquid jet high speed impingement test results 44
Figure 3-24 Lamella dimensions: a) lamella side view. b) lamella front view. c) lamella top view schematic 45
Figure 3-25 GW65 lamella spread radius measurements 46
Figure 3-26 GW65 lamella spread width measurements 47
Figure 3-27 AP2 lamella spread width measurements 48
Figure 3-28 AP2 lamella spread radius measurements 48
Figure 3-29 Non-Newtonian behaviours of AP2 49
Figure 3-30 Schematic showing jet necking and bending dimensions. 50
Figure 3-31 AP2 jet necking ratio D_n/D measurements 50
Figure 3-32 AP2 jet bending ratio L/D measurements 51
Figure 3-33 Non-Newtonian behaviour of Simu liquid jet 52
Figure 3-34 Simu jet necking ratio D_n/D measurements 52
Figure 3-35 PEO1000K liquid jet impingement: jet stretching 53
Figure 3-36 PEO4000K liquid jet impingement: jet stretching. Left: front view. Right: side view 53
Figure 4-1 GW65 average lamella thickness 56
Figure 4-2 Average lamella thickness plotted against inverse of square root of surface speed ... 56
Figure 4-3 Lamella thickness factor against jet speed. Test condition: GW65/Nzl25 57
Figure 4-4 Effects of liquid kinematic viscosity on lamella thickness factor 58
Figure 4-5 Effects of liquid jet diameter on lamella thickness factor 59
Figure 4-6 GW65 lamella spread width/radius ratio 60

Figure 4-7 Average lamella thickness plotted against a combination of jet and surface properties 61

Figure 4-8 Average lamella thickness re-plotted using convective length scale 62

Figure 4-9 Dimensionless lamella spread radius R/D 64

Figure 4-10 Dimensionless lamella spread width W/D 65

Figure 4-11 Dimensionless lamella average thickness h/D 65

Figure 4-12 AP2 lamella spread width/radius ratio 67

Figure 4-13 AP2 average downstream lamella thickness 68

Figure 4-14 Bending of streamline near impingement point 69

List of Equations

Equation 4-1 54

Equation 4-2 55

Equation 4-3 55

Equation 4-4 58

Equation 4-5 58

Equation 4-6 59

Equation 4-7 61

Equation 4-8 63

Equation 4-9 63

Equation 4-10 64

Glossary

D	Liquid jet diameter
D_0	Nozzle orifice diameter
D_n	Liquid jet necking diameter
h	Average lamella thickness
L	Liquid jet bending length
Q	Volumetric flow rate
R	Lamella spread radius
Re	Reynolds number
V_{jet}	Liquid jet speed
V_S	Surface moving speed
W	Lamella spread width
ν	Liquid kinematic viscosity

LFM	Liquid friction modifier
NBP	Nozzle back pressure
PEO	Poly(ethylene oxide)
TOR	Top of rail

GW75 75% glycerine-water solution

PGW PEO-glycerine-water solution

AP2 KELTRACK® Autopilot II liquid friction modifier

Simu KELTRACK® AP2-Simulation liquid friction modifier

45oC KELTRACK® 45oC-Simulation liquid friction modifier

Acknowledgements

First and foremost I would like to express my sincere gratitude to my graduate supervisor Professor Sheldon Green for his continuous support of my study and research, for his patience, motivation, enthusiasm and immense knowledge. Without his guidance and persistent help this thesis would not have been possible.

I would like to thank the engineers from L.B.Foster Technologies, Dr. Don Eadie, Mr. David Elvidge, Mr. John Cotter and Dr. Louisa Stanlake for their valuable technical insights and support for this project over the past two years. Their devoted work ethic and meticulous research attitude have truly inspired me.

In addition, I would like to thank Glenn Jolly and Markus Fengler for their instructive advice on designing and constructing the experimental set-ups. Their help made my ideas possible and saved me lots of time and frustration.

Finally, I would like to thank L.B.Foster Technologies and the Natural Science and Engineering Research Council of Canada for their financial support of this research.

Chapter 1: Introduction

1.1 Motivation

Rail transport is one of the most cost-effective and environmentally friendly forms of transportation in North America. The Canadian railway network, ranked the world's 5th largest rail transport network with over 46,000 kilometers of track, moves over 70 million people and more than 70 percent of total Canadian non-local surface goods every year, but only accounts for approximately 3.5 per cent of total Canadian transportation greenhouse gas emissions [1]. With rising gas prices the demand for railway transportation is expected to continue to grow. Railroads, and particularly L.B. Foster, are continually seeking means to improve the efficiency of transport by rail.

1.1.1 Friction control in railroad industry

Currently, the Canadian rail sector consumes approximately 2 billion dollars' worth of fuel and pays another $3.3 billion on track and locomotive maintenance every year [1]. One way to effectively reduce fuel consumption and maintenance cost is to distribute a thin film of appropriate friction modifying agent onto the top rail surface of conventional railroad tracks [2]. Kelsan Technologies Corporation has developed a water-based liquid friction modifier (KELTRACK®) for top of rail (TOR) friction control that has been shown in field trials with Union Pacific to reduce energy consumption by 6%, while also reducing wear on the rail and the wheel flanges by in excess of 50% [2, 3]. Other studies have shown that applying the LFM to railroad tracks leads to reduced lateral force, noise level, and more importantly, track corrugation

and damage from rolling contact fatigue [4,5,6,7], which is a major cause of derailments [8,9]. These results were further confirmed in field applications on Tokyo subway system [10,11].

1.1.2 Liquid friction modifier (LFM) and application methods

The liquid friction modifier of interest, KELTRACK®, is a water-based suspension of polymers and inorganics solids that displays non-Newtonian behaviours: shear thinning and viscoelasticity [12,2]. KELTRACK®, unlike conventional oil-based LFMs, controls the rail-wheel interface friction without compromising traction and braking [11,12].

KELTRACK® is presently dispensed from air blast atomizers on dozens of locomotives in Canada and the United States. In this form of application, the LFM is applied to the top of railroad tracks from the atomizers mounted underneath the locomotives as the locomotives move at high speeds. This form of LFM application is difficult to implement on many railroad locomotives because the required high volume, high pressure air supply may not be accessible or present at all. Air-blast spray nozzles have also been found to produce highly non-uniform rail coverage when operated in a cross-wind, as the cross-wind causes fine spray droplets to deviate from their original trajectory. Cross-winds are also known to be a major cause of nozzle fouling, likely for the same reason.

Due to the problems associated with air blast atomizers, the industry is currently seeking alternative methods to dispense LFM onto railroad tracks. One of the most viable candidate solutions is to dispense LFM by means of a continuous liquid jet stream, as liquid jets are less susceptible to crosswind effects owing to their lower drag-to-inertia ratio. Also, since the high

volume and high pressure air supply required by atomizing nozzles is no longer needed in liquid jet spraying, the resulting spraying system is more simple and robust while at the same time allowing for good control over the rate of LFM application.

1.2 Liquid jet impingement

Liquid jet impingement onto a substrate is a multiphase fluid mechanics problem of high complexity and interest in a number of technical and industrial applications. Among the applications are steel making, ink-jet printing, cooling/heating, and surface coating. The recent requirement to coat a moving surface with a liquid friction modifier (LFM) applied by a high speed jet has resulted in studies of the fundamental fluid physics of jet impingement, in order to maximize the proportion of liquid adhering to the surface following impingement. Experimental, numerical, and analytical studies have provided a vast amount of information; however, the majority of the work is concerned with parameters involved with heat transfer; little has been done to elucidate the details of the liquid flow and in particular what affects liquid jet splashing behaviour.

1.2.1 Impingement on a stationary surface

When a smooth jet of water falls vertically on to a stationary horizontal plane, it spreads out radially in a thin layer bounded by a circular hydraulic jump. Watson [13] developed a mathematical model of jet impingement which divided the flow radially into four flow regions, namely a stagnation region, a boundary layer region, a region of decreasing free surface velocity, and a hydraulic jump. Bohr et al. [14] found that the radius of a hydraulic jump increases with

increasing volumetric flow rate of the jet and decreasing liquid kinematic viscosity. With liquids of high viscosity (e.g., honey), unstable behaviors like coiling and buckling can be observed [15,16,17].

1.2.2 Impingement on moving surface

Despite its practical importance, jet impingement on moving surfaces has received little attention. Chiu-Webster and Lister [18] performed an extensive set of experiments studying steady and unsteady viscous jet impingement on a moving surface, and a model was developed for the steady flow case. A. Hlod et al. [19] modelled the flow by means of a third-order ODE on a domain of unknown length with an additional integral condition, and compared the predicted shape with experiments. However, the Reynolds numbers in these studies are much lower than those in typical railroad LFM applications.

Gradeck et al. [20] numerically and experimentally investigated the flow field of an impinging water jet on a moving substrate for various combinations of jet velocity, surface velocity, and nozzle diameters. Fujimoto et al. [21] investigated the flow characteristics of a circular water jet impinging onto a moving substrate covered with a thin film of water. However, these researchers were interested in relatively large nozzle diameters and low surface and jet velocities compared to the current work.

For high speed liquid jet impingement on high speed surfaces, Keshavarz [22] conducted a set of experiments with Newtonian and elastic liquid jets impinging on high speed surfaces and

classified the impingement into two distinct categories: deposition and splash. It was further concluded that the splash/deposition threshold was mainly determined by the Reynolds and Deborah numbers, whereas jet impingement angle and jet velocity to surface velocity ratio only had a small impact. In another study with similar jet speed and surface speed, Kumar et al. [23] performed a series of tests with several different fluids and was able to find that both increasing jet speed and increasing surface speed could transform the jet impingement from deposition to splash. They also found in tests with different glycerine-water solutions that splash only happened for solutions with glycerine concentrations of 30% to 75%, whereas deposition was always achieved with aqueous glycerine solutions of lower than 30% or higher than 75% concentration [23]. This three-regime splash/deposition pattern was also observed by Moulson in tests with aqueous glycerine solutions at lower surface speed [24]. Moulson also observed a non-continuous spattering fluid phase in the low viscosity and low surface tension regime, and thereby classified jet impingement behaviours into three categories: deposition, splash and spattering with the categories illustrated in Figure 1-1. However, the surface speeds used in the experiments discussed above did not exceed 15m/s, and the effects of surface roughness was not studied.

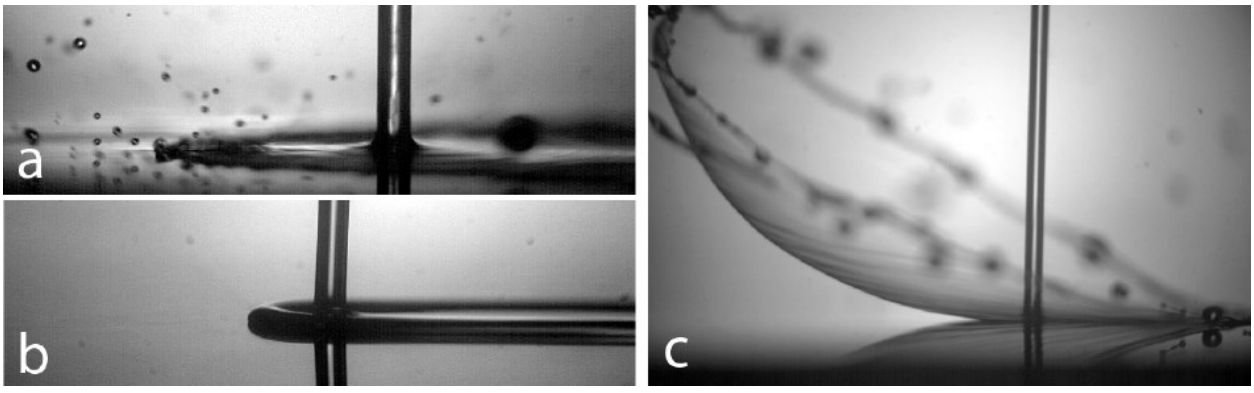

Figure 1-1 Three distinct flow regimes. (a) Spatter (b) Deposition (c) Splash [24]

To study the effect of surface roughness on jet impingement behaviour, Keshavarz [25] performed a series of experiments where a liquid jet impinged on sandpapers of different roughness. He found that, for roughness in the range of 16 microns to 400 microns, increasing the roughness height decreased the splash threshold dramatically (i.e., rougher surfaces are more prone to splash). In experiments conducted with higher surface speeds, Sterling [26] found that a splashing liquid jet could be triggered back to deposition by running the impinging jet over a short patch of slightly rougher region on the surface, implying that roughness of small heights might be able to promote deposition.

In experiments conducted with variable ambient air pressure, Moulson et al. [27] discovered that the splash/deposition threshold Reynolds number increased dramatically with decreasing ambient air pressure (i.e., lower ambient pressure makes jets more prone to deposition), while decreasing ambient air pressure below a certain level could suppress splash completely. This finding strongly suggests that the aerodynamic forces acting on the lamella plays a crucial role in causing lamella lift-off and subsequent splash. Since the air flow around the lamella is largely determined by the air/fluid interface, a more detailed study on the shape and dimension of lamella spread is justified.

1.3 Research objectives

Applying LFM to the wheel-rail interface has been proven in many studies and applications to be an effective means of controlling friction and mitigating wear, and thereby reducing fuel consumption and maintenance cost [3,4,7]. One limit on the effectiveness of LFM is that when

applied from a moving train not all of the product will adhere to the railroad tracks. The “transfer efficiency” is defined to be that portion of the dispensed product that adheres to the top of the rail. The primary thrust of this research work is to achieve the best possible transfer efficiency while providing a uniform deposition on the target surface by applying LFM in the form of a liquid jet. Thus, a better understanding of the underlying physics associated with liquid jet impingement on moving surfaces is needed.

The first objective of this research is to investigate the effects of surface velocity and jet velocity on Newtonian and non-Newtonian liquid jet impingement on moving surfaces. Since in practice trains travel at speeds ranging from 0 to in excess of 300 km/h, it is necessary to observe jet impingement at a range of train and jet speeds. The second objective is to investigate the lamella spreading and how jet speed, surface speed, and liquid properties influence its shape and size. The third objective is to investigate the effects of surface roughness of small amplitude on jet impingement. The last objective is to study the effects of liquid elasticity on the shape and behavior of the impinging jet.

Chapter 2: Methodology

2.1 Test liquids construction and characterization

A total of ten liquids were tested: seven were PEO-glycerine-water solutions prepared in the lab and the other three were commercial liquid friction modifying products produced by L.B.Foster Rail Technologies Corp. (KELTRACK® Autopilot II, AP2-Simulation and 45oC-Simulation). Among the ten test liquids, five were elastic and five were inelastic.

2.1.1 Solution preparation

PEO-glycerine-water solutions were used as sample viscoelastic fluids in the impingement tests. Glycerine is a clear, almost colorless, viscous and hygroscopic liquid with a low vapor pressure [28]. Due to its miscibility in water, it was used in the experiments to raise the viscosity of the solutions to the desired level. PEO, or poly(ethylene oxide), is a crystalline polymer of ethylene oxide. Its aqueous solution is known to be elastic [29]. PEO is highly soluble at room temperature in water due to hydration bond interaction of ether oxygens [30,31].

Although water is a good solvent for both PEO and glycerine (Mark-Houwink exponent, $a > 0.5$ [32]), PEO does not dissolve in glycerine under normal conditions, implying that polymers within the composite solvent will have smaller coil sizes and a lower intrinsic viscosity. The solutions were prepared by gradually dissolving PEO powder into distilled water under gentle magnetic stirring over a 24 hour period. PEO (Sigma-Aldrich, Canada) with viscosity-average molecular weights (MV) of one million and four million were used to create the PEO-glycerine-

water solutions. Flexible polymers like PEO are susceptible to mechanical degradation [29,33], therefore care was taken to avoid excessive agitation. Next, USP grade glycerine (99.5 wt.%, UNIQEMA, Australia) was added to the solution to raise the shear viscosity to desired level. Since PEO does not dissolve in glycerine, glycerine was added to the aqueous PEO solution gradually over a 24-hour period to avoid phase separation (Figure 2-1).

Figure 2-1 Phase separation due to PEO's low solubility in glycerine

To minimize evaporation, water absorption from ambient air and contamination, the test liquids were stored separately in air-tight containers under room temperature before and after each test. Due to the limited thermal stability of PEO [29], liquids were characterized and sprayed within five days of preparation.

2.1.2 Test liquid characterization

Table 2-1 summarizes the compositions and properties of the test liquids. Each datum in the table is an average of 6~10 measurements.

Shear viscosities were measured on a commercial rotational rheometer (Malvern Kinexus Ultra+) with various geometries. All seven of the PEO-glycerine-water solutions exhibited constant shear viscosities for shear rates ranging from 10 to 1000 s^{-1}. The three commercial LFM products showed clear rate dependent viscosities (shear-thinning). The measured viscosities of water-glycerine solutions were compared with published data [28,34] and the results showed good agreement.

Equilibrium surface tensions were measured using a du Noüy ring apparatus. The measured surface tension for de-ionized water and aqueous glycerine solutions were compared with published data and showed good agreement. The measured surface tension for PEO-glycerine-water solutions were lower than glycerine-water solutions of the same glycerine concentration due to PEO's surfactant property.

Relaxation data were measured using a commercial capillary breakup extensional rheometer (Thermofisher CaBER 1). Each liquid was tested six times on the extensional rheometer and the results exhibited a ±6% variation for most liquids. This is likely a result of inconsistent sample volume. As a sanity test, one Newtonian water-glycerine solution with known viscosity was tested on the rheometer to confirm the measured viscosity was consistent with published data.

Table 2-1 Compositions and properties of test liquids at 25°C

Liquid ID	Compositions				Properties			
	PEO M_V [g/mol]	PEO [wt.%]	Glycerine [wt.%]	Water [wt.%]	Density [g/ml]	Viscosity [cp]	Surface Tension [mN/m]	Relaxation Time [ms]
GW65	-	0	65	35	1.164	12.87	66.68	
GW70	-	0	70	30	1.176	17.57	65.66	-
GW80	-	0	80	20	1.192	46.67	64.84	-
GW85	-	0	85	15	1.210	77.63	64.01	-
GW90	-	0	90	10	1.232	106.43	63.58	
PGW1000K	1,000,000	0.15	50	49.85	1.113	12.03	52.24	8.29
PGW4000K	4,000,000	0.15	50	49.85	1.111	17.04	52.86	43.7
AP2	-				1.079	Rate-dependent	32.92	911
Simu	-				1.015	Rate-dependent	33.51	765
45oC	-				1.104	Rate-dependent	33.77	248
Measurement Uncertainty					±1%	±1%	±3%	±6%

2.2 Flow rate test methods

Preliminary experiments on the spray system were conducted with the test liquids at different nozzle back pressure to gain essential information of liquid jet properties: jet diameter, jet speed and volumetric flow rate. Due to the difficulty associated with accurately measuring sprayed liquid volume, mass flow rate were recorded instead and then used to calculate volumetric flow rate.

2.2.1 Mass flow rate measurement

To measure the mass flow rate, flow was permitted to the nozzle through the activation of an upstream solenoid valve for a duration of two seconds. During this period of time, the resultant liquid jet was deflected by a flow-interrupter to remove any potential transient effects associated with the initiation of the jet from the nozzle. Following this, the flow-interrupter, driven by a fast-response solenoid, was de-activated quickly to let the liquid jet flow freely into a beaker for collection. For each measurement, the jet flow was permitted for 20 seconds before the flow-interrupter was activated again to deflect the flow from the beaker. The solenoid valve was then turned off shortly after.

The weight of the sprayed liquid was measured on a precision balance. Combining that with an average nozzle back pressure recorded during the 20-second jet flow, a graph could be plotted for each liquid/nozzle combination to show mass flow rate characteristics.

2.2.2 Liquid jet diameter measurement

The diameter of the liquid jet coming out of a nozzle is measured using imaging method. Figure 2-2 illustrates the jet diameter measuring method, where the scale of the image is calibrated by measuring a laser printed micro-ruler in the image. Liquid jet diameter was measured for each liquid/nozzle combination at variant nozzle back pressures to ensure accuracy.

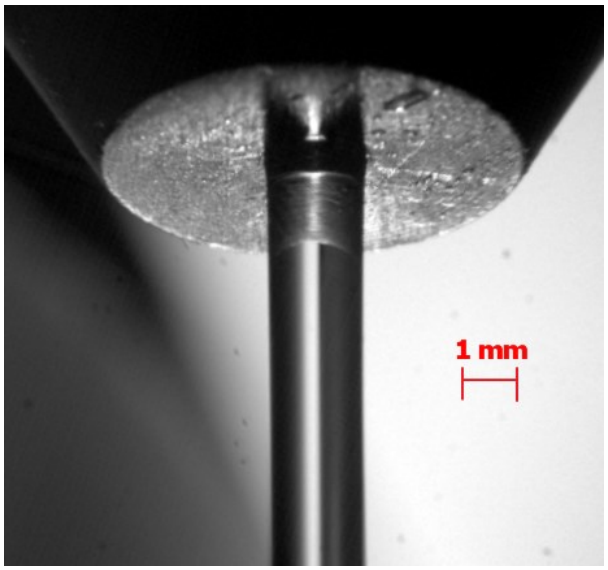

Figure 2-2 Jet diameter measurement using imaging method. Nozzle diameter: 1854 µm.

2.3 Lab experiment method

As mentioned in the previous chapter, in field applications the liquid friction modifiers are applied to the top of railroad tracks by means of a spray nozzle mounted underneath a locomotive or a Hi-Rail truck. In these applications, the moving nozzle applies the LFM onto a stationary rail. However, in a lab environment, it would be extremely difficult given space limitations to replicate a similar scenario. Therefore, experimentation was done with stationary nozzles applying LFM onto moving rail surfaces.

The main concern from this approach is the obviously different surrounding air flow field relative to the field application. In the lab environment the rail surface moves in a rather still surrounding flow field, leading to the formation of a boundary layer on top of the surface, whereas in field applications, with the locomotive taken as an inertial frame of reference, the mean air flow moves at the same velocity as the railroad track (provided that the ambient air is still relative to the ground). Figure 2-3 further illustrates the difference described above. This moving flow field difference could affect the jet impingement on the following scales:

i. Macro-scale influence: Cross-wind could deflect the liquid jet or cause the liquid jet to breakup under extreme conditions.

ii. Micro-scale influence: Aerodynamic forces inside the boundary layer could change the lamella shape and thereby affect impingement behaviour.

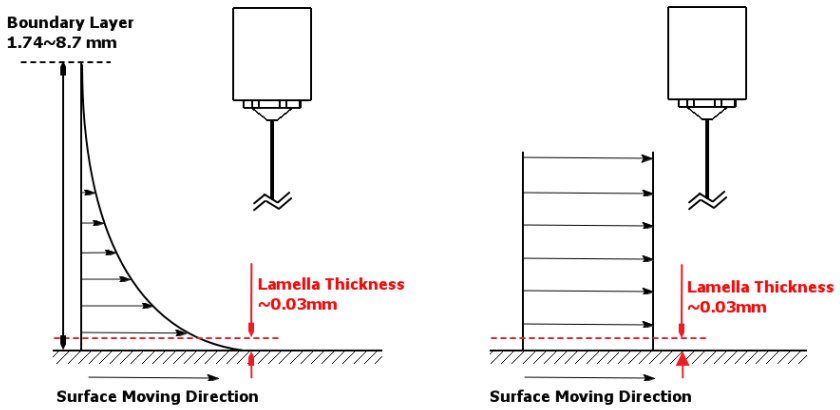

Figure 2-3 Simplified boundary layer profiles. Lab environment (left) vs. field environment (right)

To examine the macro-scale effects, an experiment where the nozzle was mounted inside a wind tunnel was done to show that with a nozzle back pressure over 35 psig jet deflection was insignificant and jet breakup never happened. A field trial carried out by L.B. Foster Rail Technologies Corp. in the summer of 2012 showed the same result.

For a rough estimate of micro-scale effects, the laminar boundary layer assumption was employed to calculate the boundary layer thickness to be 1.7~8.7 mm for a 5~25 m/s surface speed. This means that the lamella, typically around 30~120 microns thick, lies in the bottom 5% region of the boundary layer, where the air velocity is nearly the surface velocity (Figure 2-2). For example, for a Blasius boundary layer the difference between local air velocity and the surface velocity is within 4% at a height of 0.02δ above the surface. Therefore, the boundary layer formed on top of the surface in lab environment should not have a major impact on the jet impingement behaviour. Also, the above analysis assumed 'perfectly still air' in field applications, which is an oversimplification. In real applications, the locomotives accelerate the air in the gap between the train and the rail to 70%-90% of the locomotive speed as they move, which makes the situation even closer to the lab experiments [35]. A detailed study of full scale train underbody air flow is currently being carried out by another researcher at UBC.

2.4 Experimental apparatus for low speed impingement tests

For low to moderate speed tests, a linear traverse system was used to provide a moving surface onto which a liquid jet could impinge. The linear traverse is a pneumatic-energy-powered system designed to accelerate to the desired speed a section of steel plate, representing the rail surface, mounted on top of a wood projectile.

2.4.1 Air cannon set-up

Figure 2-4 depicts the linear traverse, which consists of a 30 gallon air tank (200 psig capacity, with a safety valve set at 150 psig) connected to a central air compressor (not shown in the figure) capable of delivering a maximum of 100 psig, a solenoid actuated poppet valve

connected to the tank by means of a 1.5” NPT rubber hose, a 3 meter long 10 cm x 15 cm x 0.6 cm section of rectangular steel tubing, with the last meter of the tube being cut in half crosswise, and a stop mechanism.

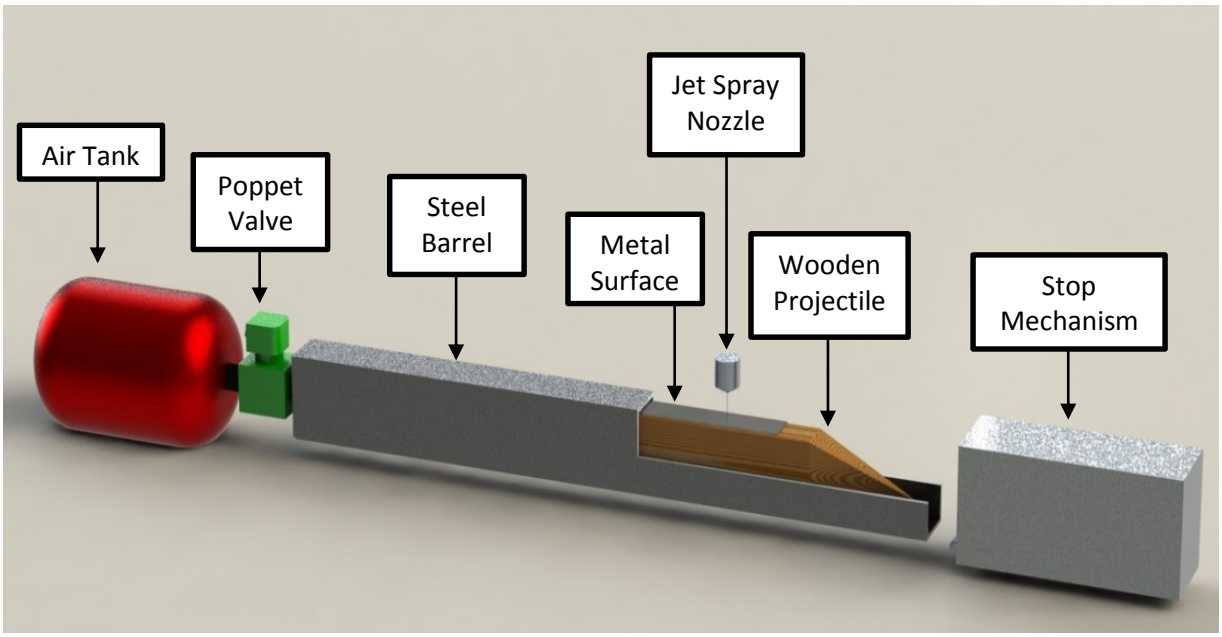

Figure 2-4 Schematic of air cannon test set-up for low speed impingement testing

The system works as follows. The projectile, which is a wooden carrier base with a metal impaction surface mounted on top, is inserted into the barrel. The spray nozzle is opened and then the poppet valve is opened quickly, permitting pressurized air in the tank to be rapidly released into the long, narrow barrel. The rapid pressurization of the barrel behind the projectile forces the projectile out at a velocity that is dependent on the initial air pressure set in the tank. After exiting the barrel, the projectile travels beneath the nozzle, allowing the liquid jet to impinge on the surface mounted on top. After passing under the liquid jet the projectile hits a stopping mechanism that was designed to dissipate the projectile’s kinetic energy in a controlled deceleration to reduce damage to the projectile and ensure safety. The linear traverse can propel a 1.5 kg projectile up to a speed of 25 m/s using an air pressure of 60 psig.

2.4.2 Impingement surfaces and wooden carrier (projectile)

Previous work done by G. Sterling [26] and B. Keshavarz [25] found that roughness of the moving surface has an influence on jet impingement. To find the appropriate surfaces for testing, surface roughness information for a total of nine 304 stainless steel plates were measured on a commercial profilometer. Among the nine metal plates, three had standard machine-produced industrial finishings (a brushed #3, a brushed #4 and a mirror-like #8), five were #8 mirror-like stainless steel plates abraded by sandpapers of different grit numbers (identified as P followed by grit number used to produce it, e.g. P60, P220 etc.), and one was unpolished cold-rolled sheet steel plate (identified as 2B). The roughness of each metal plate was measured 12 times and in different directions on the profilometer to average out effects of randomness in distribution of the surface features. Figure 2-5 shows two metal plates with a demonstration of the measuring patterns.

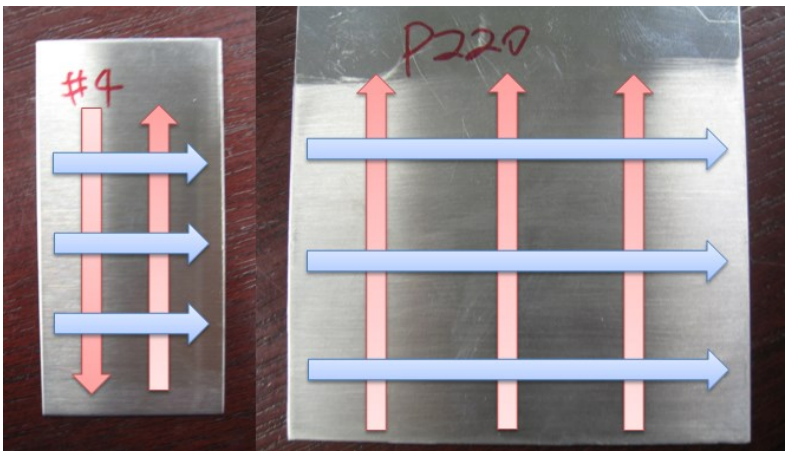

Figure 2-5 Illustration of surface roughness measuring patterns

Figure 2-6 shows the measured roughness of each metal plate. The first three surfaces, although with smaller roughness deviations, were not suitable for our tests because the highly directional roughness patterns required highly consistent test conditions, i.e. any subtle rotation or

misalignment of the projectile to the nozzle could result in a huge variation in 'actual' surface roughness. Roughness of the sandpaper-blasted surfaces, on the other hand, were less direction-dependent and showed a clear decreasing trend with increasing grit numbers. Typical short-wavelength railroad track roughness height ranges from 0.15 μm to 0.7 μm depending on different local railroad standards and last maintenance date [35,36]. With these in mind, three surfaces were chosen for use in the jet impingement tests. Table 2-2 lists the surfaces used for the air cannon tests.

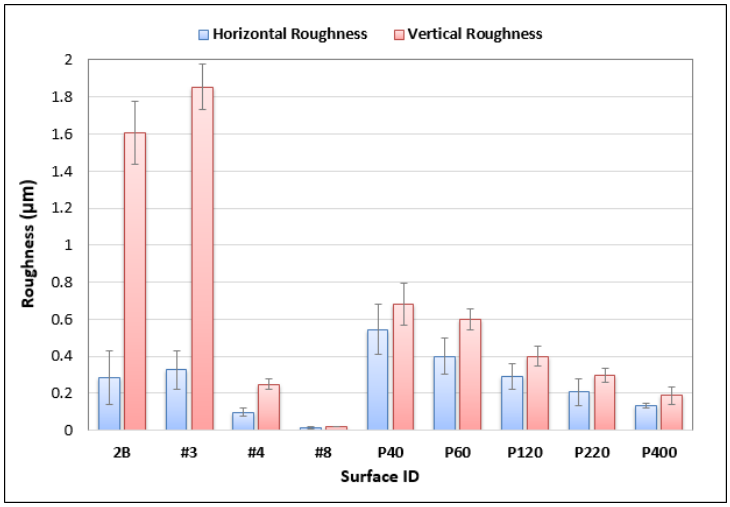

Figure 2-6 Measurements of surface roughness for nine different stainless steel plates

Table 2-2 Three stainless steel surfaces chosen to represent typical railroad track

Surfaces		Roughness height (μm)		
Type	ID	Horizontal	Vertical	Average
Mirror	#8	0.013	0.020	0.0160
Smooth	P400	0.130	0.187	0.1583
Rough	P60	0.378	0.631	0.5050

The prepared metal surfaces were mounted to a wooden base (the wooden projectile). This wooden base acted as a light-weight carrier for the impaction surface. The dimensions of the wooden projectile were chosen to match closely those of the steel barrel internals to minimize air

leakage. A 1/8” thick soft rubber sheet secured tightly in between two layers of plywood was added to the back of the projectile to act as a ‘wiper’ to further ensure the tight seal around the inside of the barrel. The leading 20 cm of the projectile was shaped into an aerodynamic nose with a barb underneath so that the stop mechanism would catch it securely without it bouncing back. The top surface of the projectile was divided into three sections with 1-inch-long gaps in between so that three metal surfaces could be impinged on by the liquid jet in one test with minimal interference. One projectile used in the test is shown in Figure 2-7.

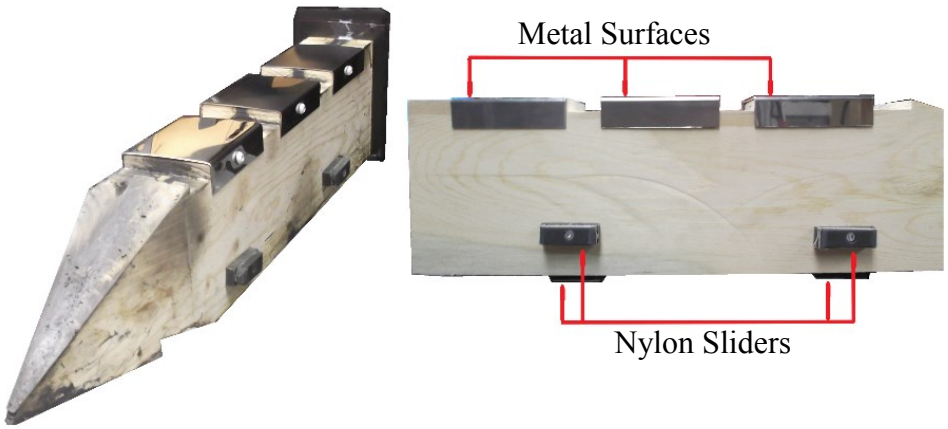

Figure 2-7 A wooden carrier (projectile) with three surfaces mounted on top used for low speed tests

2.4.3 Spray system

The nozzle used in this work had a 648 micrometers diameter circular orifice. The jet flow was driven by a pressurized bladder accumulator that provides a nozzle back pressure of up to 200 psig. A pressure transducer installed immediately upstream of the nozzle was used to record the nozzle back pressure. A solenoid valve was employed to control the flow. An advantage of this setup was its ability to provide more stable nozzle back pressures than pumps, because it contained no moving components anywhere between the liquid reservoir and the jet.

2.4.4 High-speed imaging system

Vision Research's Phantom v611 high-speed cine camera was employed to visualize jet impaction on the projectile surface. This camera uses a fast wide screen CMOS sensor to allow image capture at extremely high frame rates and high resolutions. A 1kw high-intensity incandescent light source was used to illuminate the field of view. To achieve an evenly illuminated background, a light diffusor sheet was placed between the light source and the impingement point. Figure 2-8 illustrates the imaging setup used in the experiments. A number of camera lenses and settings were tested during the preliminary experiments, and a *Navitar Zoom 7000* lens stood out to best satisfy our requirements for field-of-view and depth-of-field. Two camera settings were used, one with 800x600 resolution and 10,000 fps for HD imaging and the other with 500x350 and 30,000 fps for fast imaging. In either case, the camera RAM could store up to one second of test video.

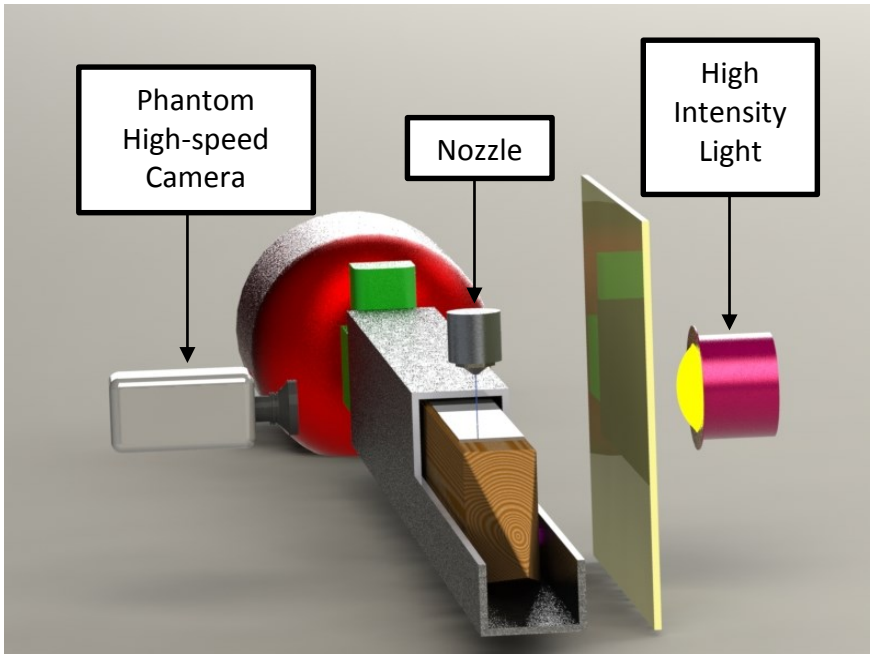

Figure 2-8 Imaging set-up for recording high-speed videos with Phantom V611 camera

2.4.5 Electrical control system

At a 25 m/s surface (projectile) speed, the jet impinges on the surface for around 10 milliseconds. Although the high speed camera was able to capture around 900 milliseconds of video, triggering the camera manually at the right moment to capture the impingement was still a challenging and often unsuccessful task. Also, turning on the nozzle and light too early could result in test liquids building up in the barrel, which could affect projectile movement. To solve these issues, an electrical control system based on a National Instrument Data Acquisition 6009 was designed and built. The control system (Figure 2-9), mainly comprised of an optic sensor placed at the opening of the barrel and a control box connected to a computer, was able to detect projectile movement and automatically turn on and off the spray nozzle, light source and high speed camera, as well as record nozzle back pressure during impingement at exactly the right time. This system allows the operator to conduct a test by pushing one button instead of controlling several devices manually at the same time.

Figure 2-9 Electrical control system

2.4.6 Safety considerations

To improve safety an aluminum cage was built to surround the projectile path between the barrel exit and the stop mechanism and prevent any damage in case of a projectile derailment. Another, possibly better, way to meet the laboratory safety requirements was to redesign the projectile and barrel so that the projectile movement could be strictly constrained on a linear path with no possibility in deviation. One example of such projectile/barrel design is given in Figure 2-10. These designs, although able to offer more stability during a test and more consistency between tests, were not carried out due to limited time and budget.

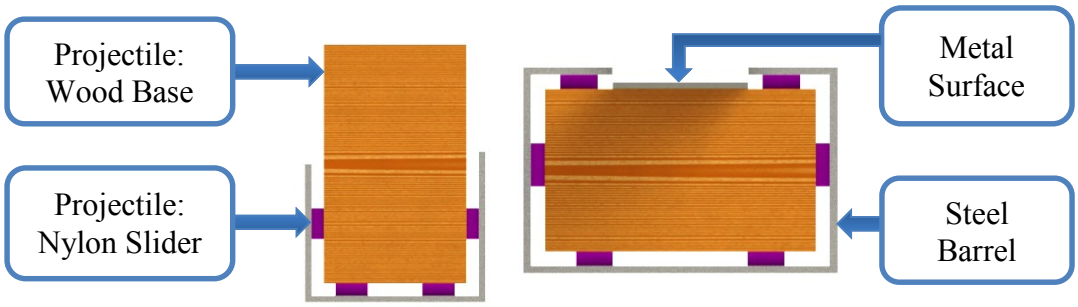

Figure 2-10 Cross sectional views of projectile/barrel designs:

(Left) Current design where the projectile might move up and deviate from the desired linear path
(Right) Example of a better design where the projectile movement is fully constraint on the linear path

The completed air cannon, which is able to propel a 1.5 kg projectile to over 25 m/s in less than 0.1 second, could be a dangerous apparatus if operated by inexperienced or careless users. Therefore, a cannon control panel was built to ensure that the cannon system could only be turned on with keys held by experienced users. To avoid firing the cannon by accidentally hitting a button, the control panel also featured a safety lock that required the operator to use both hands at the same time for firing the cannon.

2.5 Experimental apparatus for high speed impingement tests

The air cannon was not able to provide a stable and linear surface speed higher than 25 m/s. Therefore, a spinning disk test set-up was employed for high speed tests.

2.5.1 Spinning disk set-up

The spinning disk test set-up consists of a well-balanced 63 cm diameter polished steel disk 3 cm thick (Figure 2-11). The disk, driven by a variable frequency drive (VFD) motor, was able to spin at 500 to 3000 rpm, giving a surface speed of 15 to 100 m/s at the impingement point (at a radius of 30 cm). The disk surface was finished to resemble a typical rail top roughness.

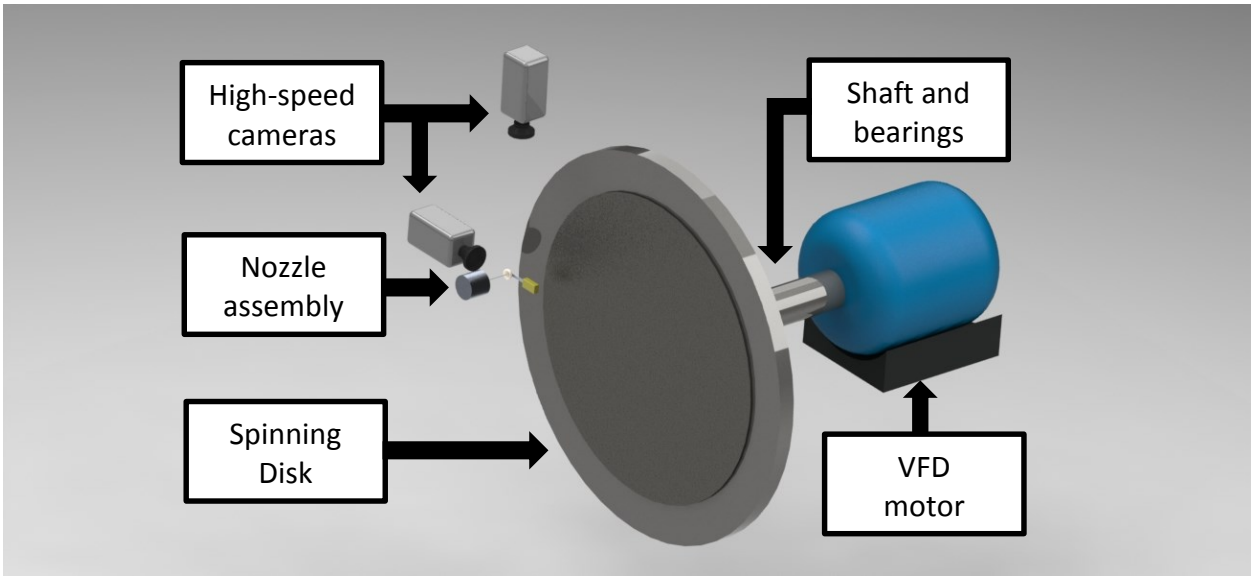

Figure 2-11 Schematic of spinning disk with two-camera imaging set-up illustration

A spray system similar to the one employed in the air cannon test set-up was used to generate the liquid jet. A solenoid-actuated flow interrupter (see Figure 2-12) was placed in front of the nozzle so that the jet impinges on a surface that has not been wetted during a prior revolution.

2.5.2 High-speed imaging system

Two cameras (a Phantom V611 high-speed camera and a Phantom V7 high-speed camera) were used in high speed tests to record impingement behaviours from two different angles at the same time. With the disk spinning clockwise and the jet impinging at the 9 o'clock position on the disk, the camera placed above the impingement point recorded the front view of the jet impingement, and a second camera recorded the side view of the jet impingement. Two separate lighting systems (not shown in the figures) were used to illuminate both cameras' fields-of-view. Imaging done with the side view made use of a high intensity fiber optic light source (MO150, JH Technologies) which was able to locally illuminate the impingement site without conflicting with the axle. Meanwhile imaging done from the front made use of a high intensity 100 watt 6700 Lumen white LED array with collimating lens. For both camera angles, to protect the camera lens from fluids leaving the surface of the disk as well as to provide a clear viewing window after each test, a sheet of acetate film was placed in front of the camera lens. Both cameras were set at 500x500 resolution and 30,000 fps for high-speed imaging.

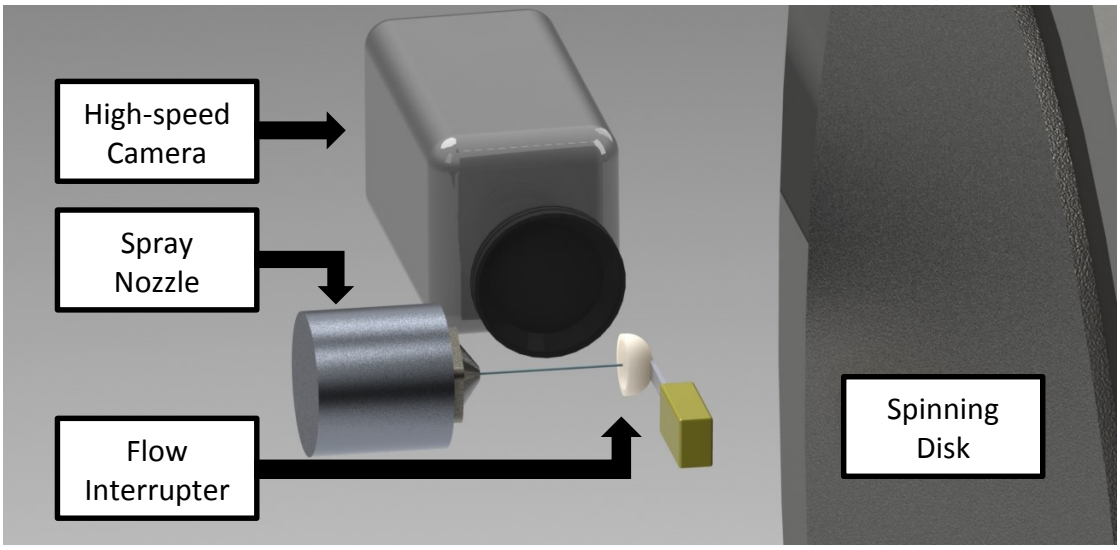

Figure 2-12 High-speed imaging set-up for side view video recording

2.5.3 Safety considerations and electrical control system

To protect users from accidentally contacting the disk while in operation and to confine all test fluids during an experiment, a polycarbonate safety enclosure was built over the disk and spray system (Figure 2-13). Doors enabled access to the disk as well as the interior of the enclosure for servicing, adjustments and cleaning of the viewing windows, nozzle assembly and disk. A vacuum cleaner was connected to the bottom of the safety enclosure, where all the test liquids and water/organic solvent used for cleaning were directed after each test.

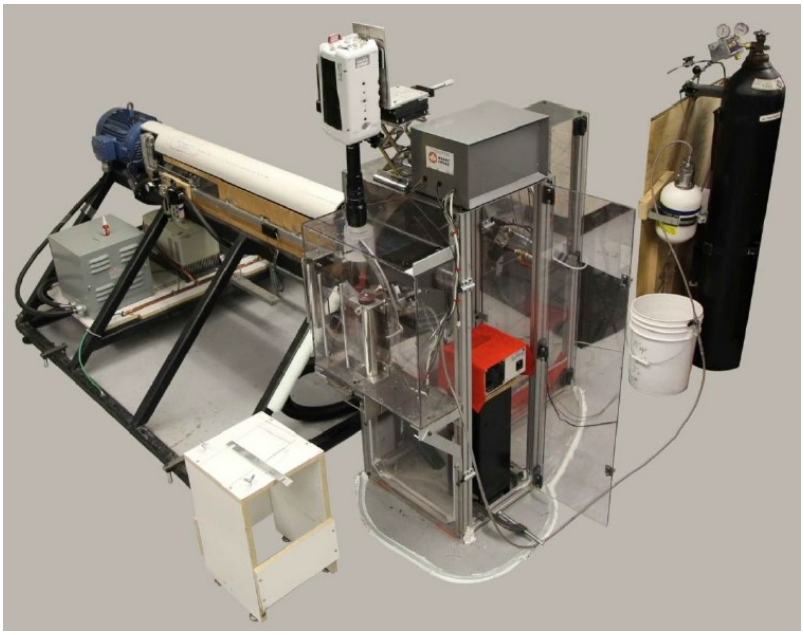

Figure 2-13 Photograph of the experiment apparatus used for high-speed tests

For the same reason as in the air cannon tests, a control system was employed to control all the devices used in each test: the two high-speed cameras, the two lighting systems, the spray system, and an automatic cleaning system that could clean and dry the surface as well as remove used liquids. The disk speed could be set with an RS232 module that interfaced between a computer and the variable frequency drive motor. With the control system set up, users could run a test with one click.

Chapter 3: Results

3.1 Liquid jet properties

Preliminary experiments on the spray system were conducted with the test liquids at different nozzle back pressure to gain essential information of liquid jet properties: jet diameter, jet speed and volumetric flow rate.

3.1.1 Flow rate test results

Figure 3-1 reports results of flow rate tests conducted on a nozzle with an orifice diameter of 648 μm. Test liquids used in these tests were PEO-glycerine-water solutions. Details of the test liquid properties can be found in Table 2-1. Power law fits for the data are presented in Table 3-1 in the form of $y = a(\Delta P)^k$. Solutions of higher viscosity show lower flow rate due to higher viscous losses at the orifice. Of the two elastic liquids, PEO 4000K displays strong non-Newtonian behaviour. This is likely caused by asymmetric vortex growth inside the nozzle [38]. The discharge coefficient for water-glycerine solutions was calculated as a function of the Reynolds number and is plotted in Figure 3-2.

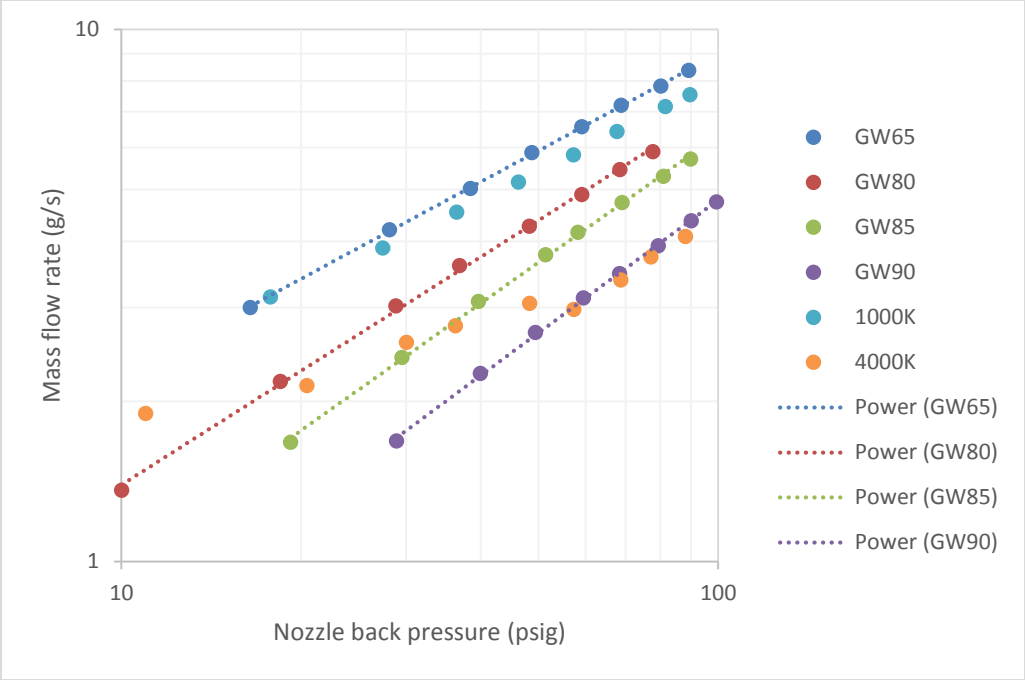

Figure 3-1 Model elastic and inelastic liquids mass flow rate test results. Nozzle orifice diameter: 648 µm.

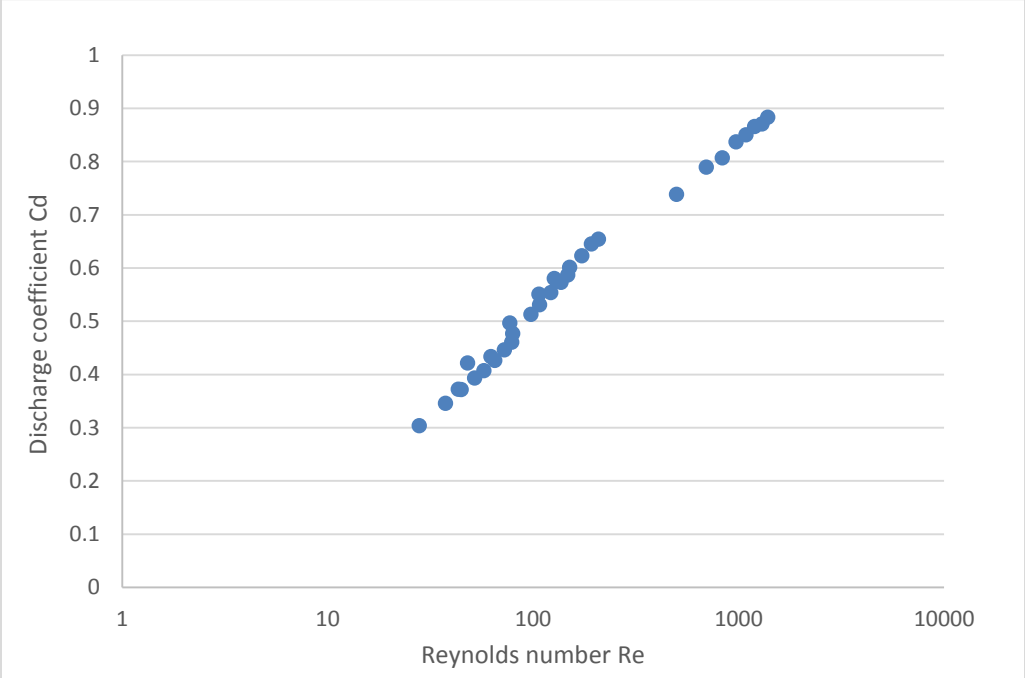

Figure 3-2 Discharge coefficient for water-glycerine solutions as a function of Reynolds number

Table 3-1 Empirical fit parameters: same nozzle, different liquids

Test liquid	a	k	R^2
GW65	0.555	0.6048	0.9998
GW80	0.2711	0.711	0.9989
GW85	0.1639	0.7931	0.9989
GW90	0.1055	0.8279	0.9993

Figure 3-3 reports results of mass flow rate tests conducted on a series of nozzles with different orifice sizes. In these tests, 85% aqueous glycerine solution was used. Table 3-2 lists the nozzles used in these tests and empirical fitting parameters of the data in the form of $y = a(\Delta P)^k$. Smaller nozzles provide lower mass flow rate per area due to higher viscous loss at the orifice.

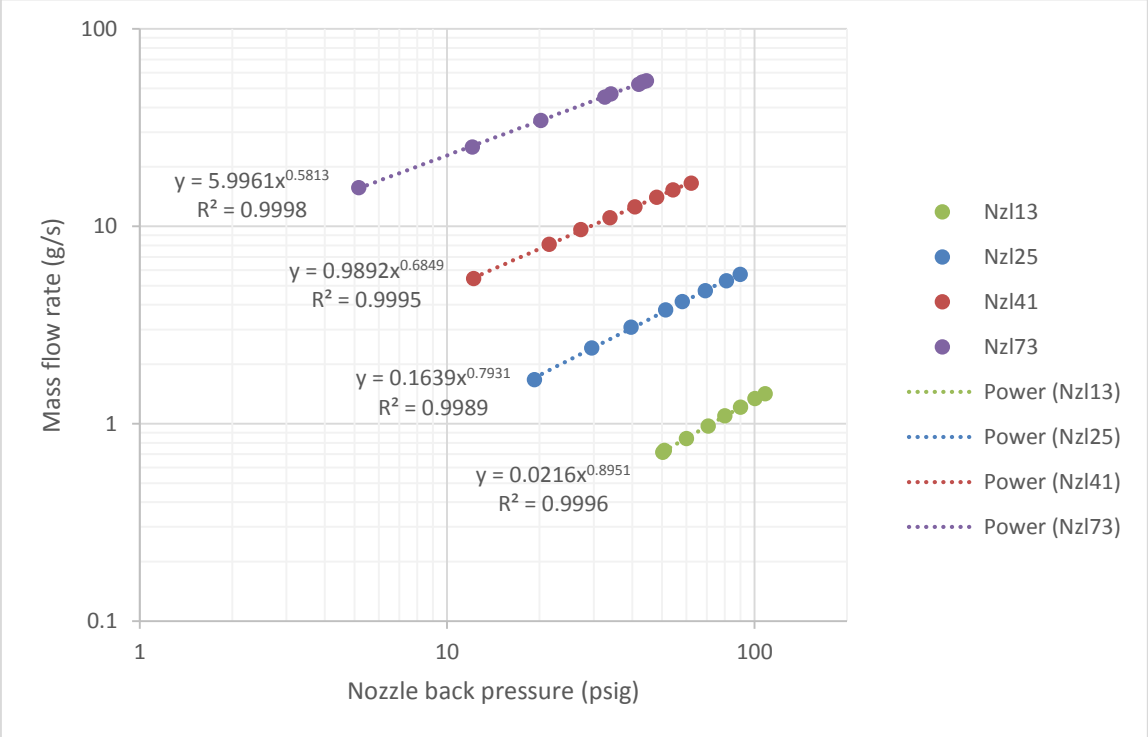

Figure 3-3 Mass flow rate test results: 85% aqueous glycerine solution, varying nozzle orifice diameters.

Table 3-2 Empirical fit parameters: same test liquid, different nozzle sizes

Nozzle orifice diameter	a	k	R^2
1855 µm	5.9961	0.5813	0.9998
1041 µm	0.9892	0.6849	0.9995
648 µm	0.1639	0.7931	0.9989
340 µm	0.0216	0.8951	0.9996

Figure 3-4 presents results of mass flow rate tests of three commercial liquid friction modifiers. The 648 µm nozzle was used in these tests. While all three liquids behave similar in terms of mass flow rate characteristic, 45oC shows slightly higher flow rate due to reduced viscosity.

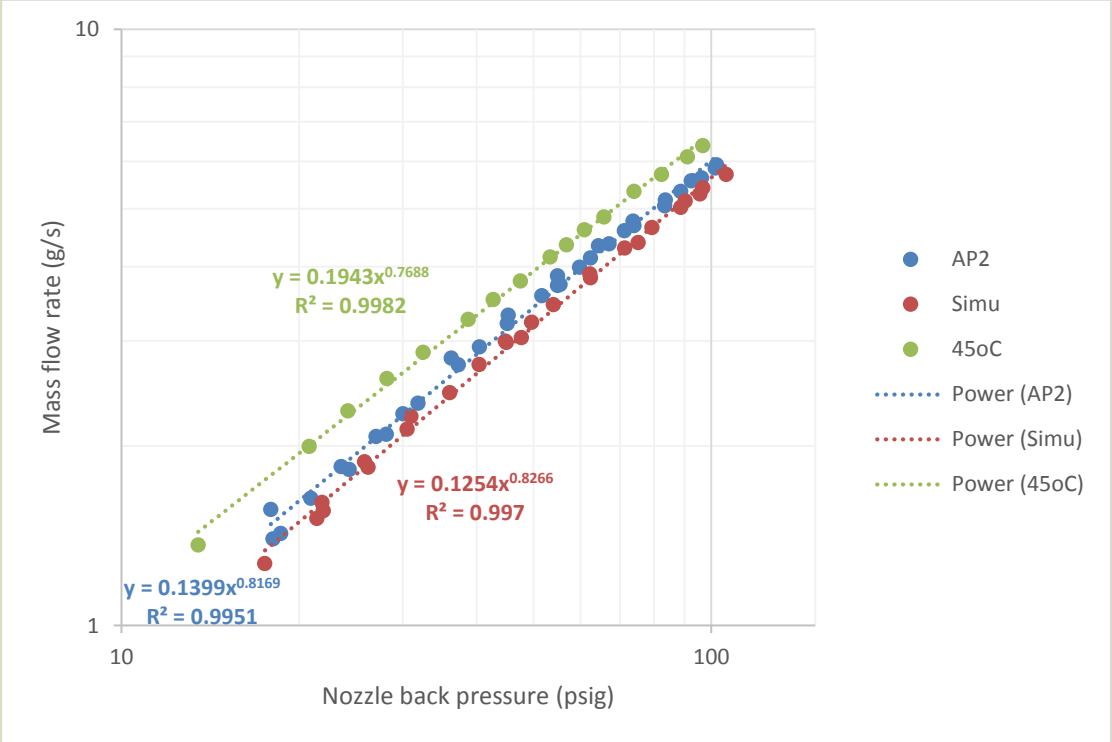

Figure 3-4 Mass flow rate test results for commercial LFMs. Nozzle orifice diameter: 648 µm.

3.1.2 Liquid jet diameter measurements

The results of liquid jet diameter measurements are presented in Table 3-3. Liquid jet diameter were measured at six different nozzle back pressures and the results showed that liquid jet diameter is independent of nozzle back pressure for the liquids tested. In the table, each data is an average of the six measurements.

In the table, the D_j/D_0 ratios are close to $\sqrt{3}/2$ for all but the largest nozzle, indicating a fully-developed Poiseuille profile right at the nozzle exit [41]. The D_j/D_0 ratio for the largest nozzle is larger because its reduced orifice length to diameter ratio is not enough for the flow to become fully-developed before exiting the nozzle.

Table 3-3 Nozzle diameter and liquid jet diameter measurement.
(Test liquid: 85% glycerine-water solution)

Nozzle	Orifice diameter D_0 (μm)	Jet diameter Dj (μm)	Dj/D_0
Nzl73	1854	1762	0.950
Nzl41	1041	902.6	0.867
Nzl25	647.7	564.7	0.871
Nzl13	326.5	281.3	0.862

With knowledge of the liquid density, mass flow rate and jet diameter secondary properties like the volumetric flow rate and liquid jet speed can be calculated.

3.2 Effects of surface roughness on liquid jet impingement

To better understand the effects of surface roughness on liquid jet impingement, a series of tests were performed with different liquids on three stainless steel surfaces with different roughness levels: rough finish, smooth finish and mirror finish, representing rough railhead, smooth railhead and ultra-smooth surface, respectively.

3.2.1 Commercial LFMs

Three types of commercial LFMs were used in these tests: AP2, 45oC and Simu. AP2 impingement test results on mirror surface (0.016 μm), smooth surface (0.158 μm) and rough surface (0.505 μm) are presented in Figure 3-5, Figure 3-6 and Figure 3-7, respectively. These tests were performed on the air cannon test set-up with the three-surface projectile to ensure the tests were done with the same jet and surface speed. The 648 μm nozzle was used for these tests. In the three graphs, each scatter point represents one test result. Conditions of the test (surface speed and jet speed) are x and y coordinates. The colour of the scatter point indicates result of the test at these conditions (green for deposition, red for splash). For example, a green scatter point at (15,20) indicates deposition was achieved in a test at 15 m/s jet speed and 20 m/s surface speed, while a red scatter point at (21,25) indicates splash occurred in a test at 21 m/s jet speed and 25 m/s surface speed.

Figure 3-5 shows that on ultra-smooth mirror surface, splash happens at high surface speed and high jet speed, while test conducted at same jet and surface speed on the other two surfaces achieved deposition, as shown in Figure 3-6 and Figure 3-7, indicating small roughness heights may supress splash.

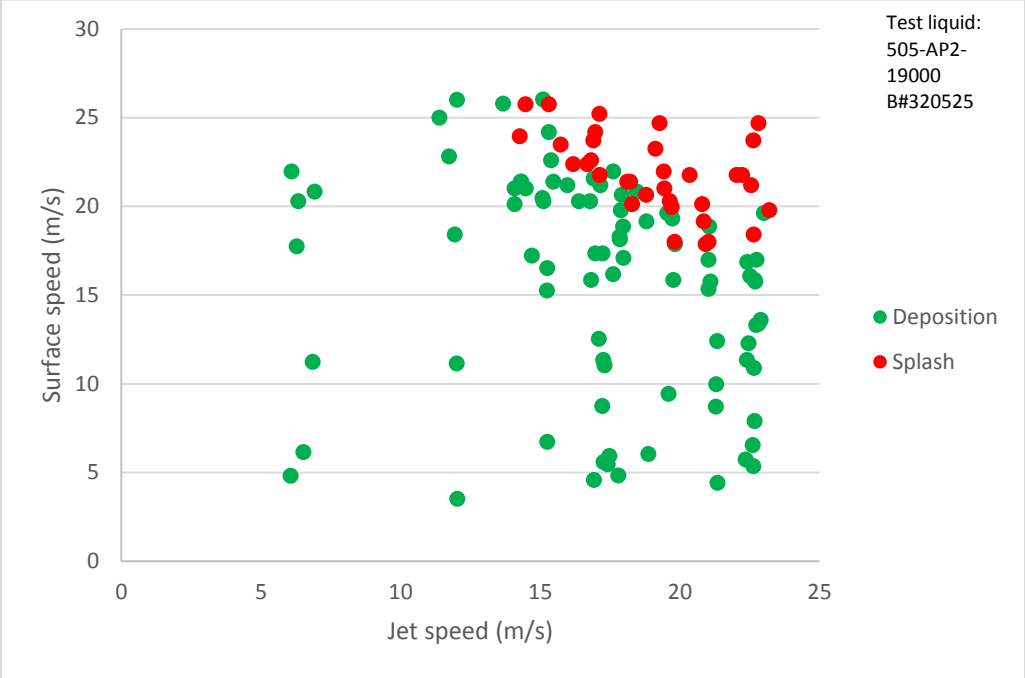

Figure 3-5 AP2 liquid jet impingement on mirror surface test results

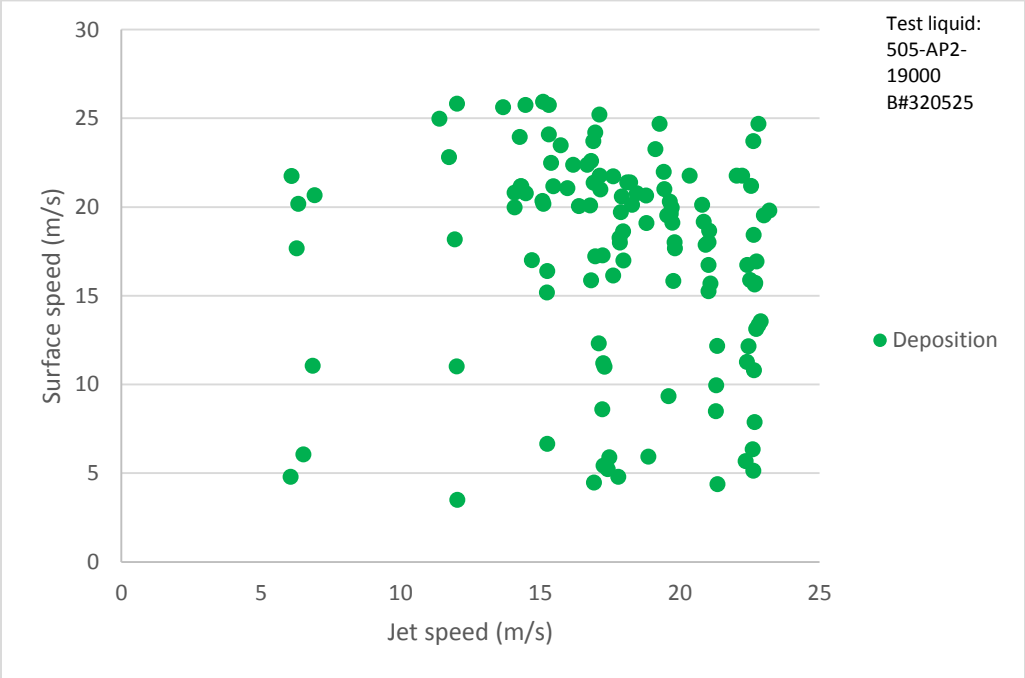

Figure 3-6 AP2 liquid jet impingement on smooth surface test results

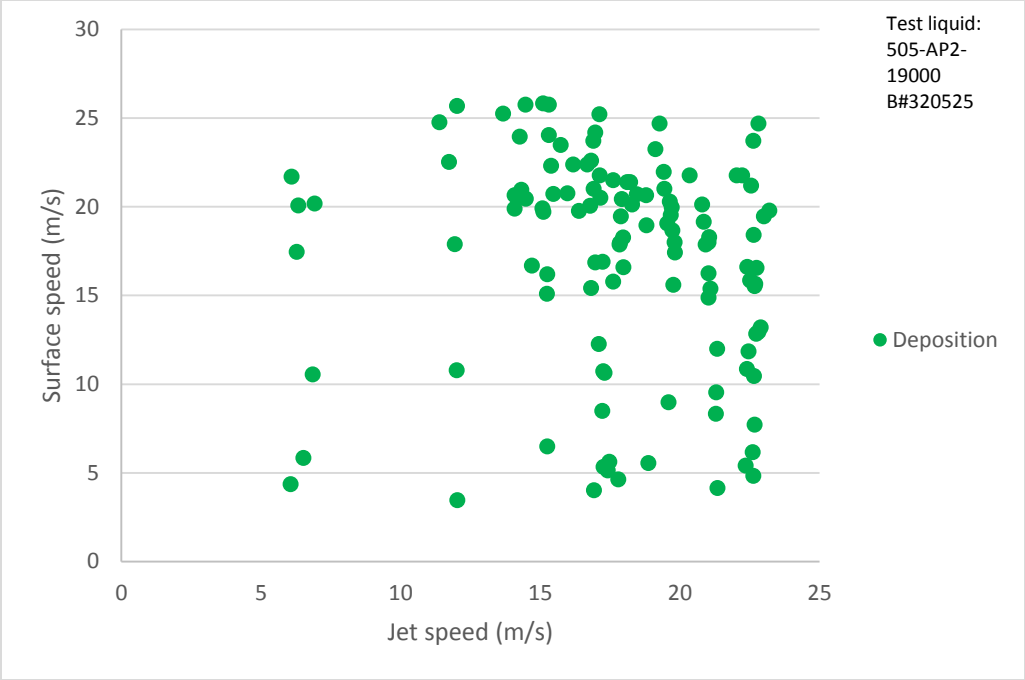

Figure 3-7 AP2 liquid jet impingement on rough surface test results

Figure 3-8 and Figure 3-9 plot the results for experiments performed with 45oC at variable jet and surface speed on the three surfaces. The same 648 µm nozzle was used in these tests. Since 45oC is a reduced viscosity version of AP2, its splash/deposition characteristic on the mirror surface, as shown in Figure 3-8, is also similar to that of AP2, except for a lower jet and surface speed threshold and a larger overlapping area in between splash region and deposition region. In the overlapping area, liquid lamella is highly unstable, therefore any tiny disturbance (e.g. imperfection on surface or jet) may turn a deposition into splash. Examples of such occurrences are shown in Figure 3-20 and Figure 3-21.

As for AP2, with the 45oC liquid splash only occurs at high jet and surface speeds on the mirror surface, while tests done at same conditions on the other two surfaces show no splash.

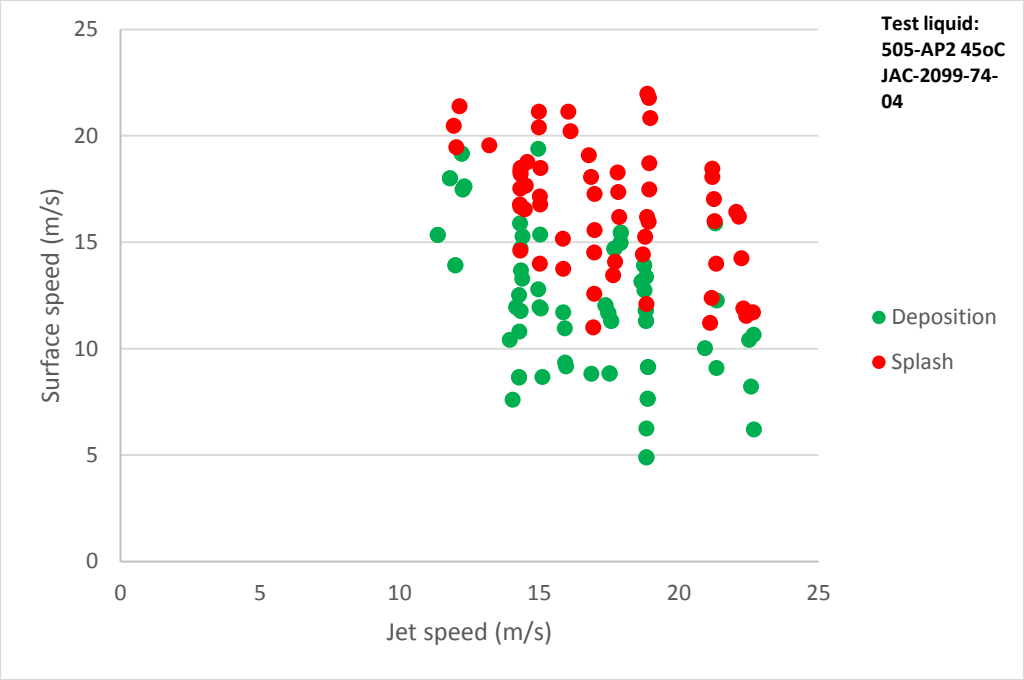

Figure 3-8 45oC liquid jet impingement on mirror surface test results

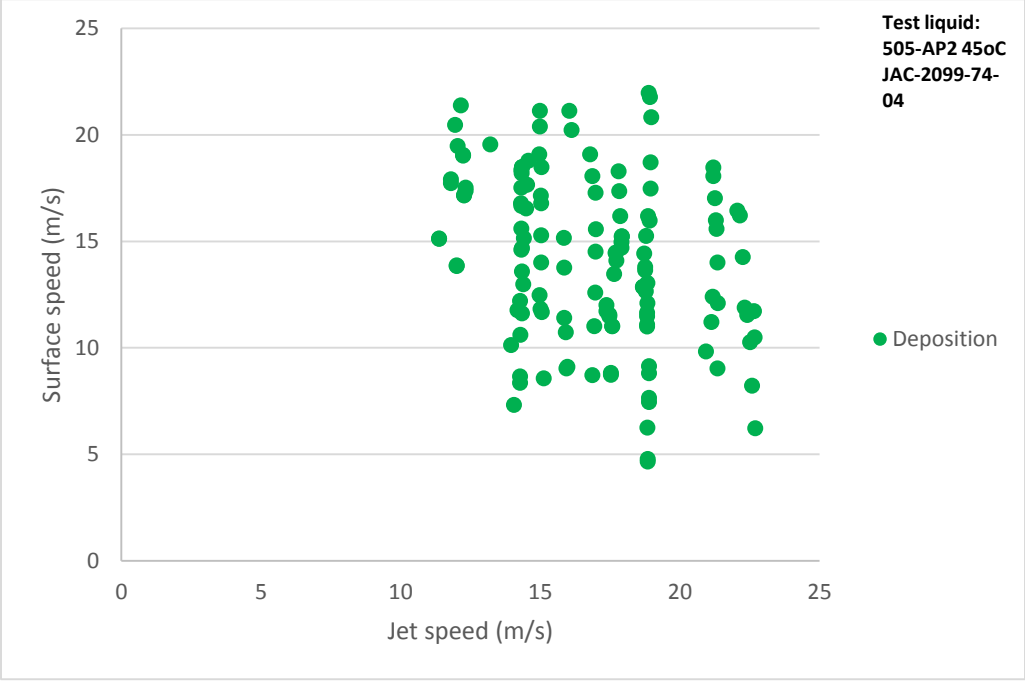

Figure 3-9 45oC liquid jet impingement on smooth surface test results

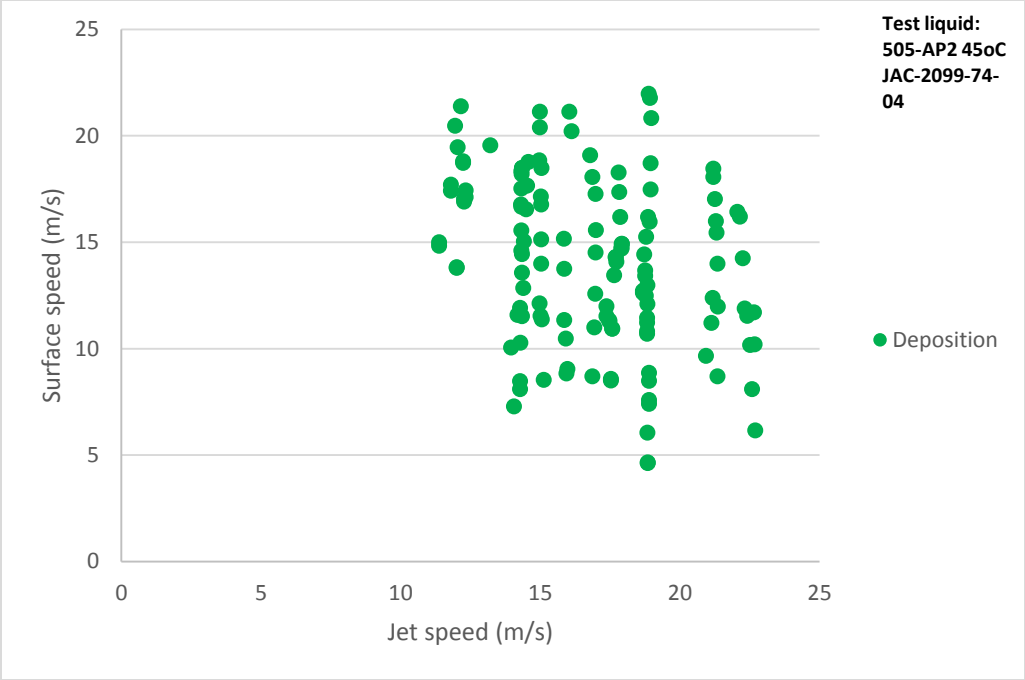

Figure 3-10 45oC liquid jet impingement on rough surface test results

Figure 3-11, Figure 3-12 and Figure 3-13 plot the results for experiments performed with Simu at variable jet and surface speed on the three surfaces. The same 648 µm nozzle was used in these tests. On the mirror surface, splash occurs at high jet speed and low surface speed, while on the other two surfaces, no splash is observed. Comparing Figure 3-5 and Figure 3-11 shows that the simulation liquid did not mimic well the AP2 liquid in terms of splash threshold.

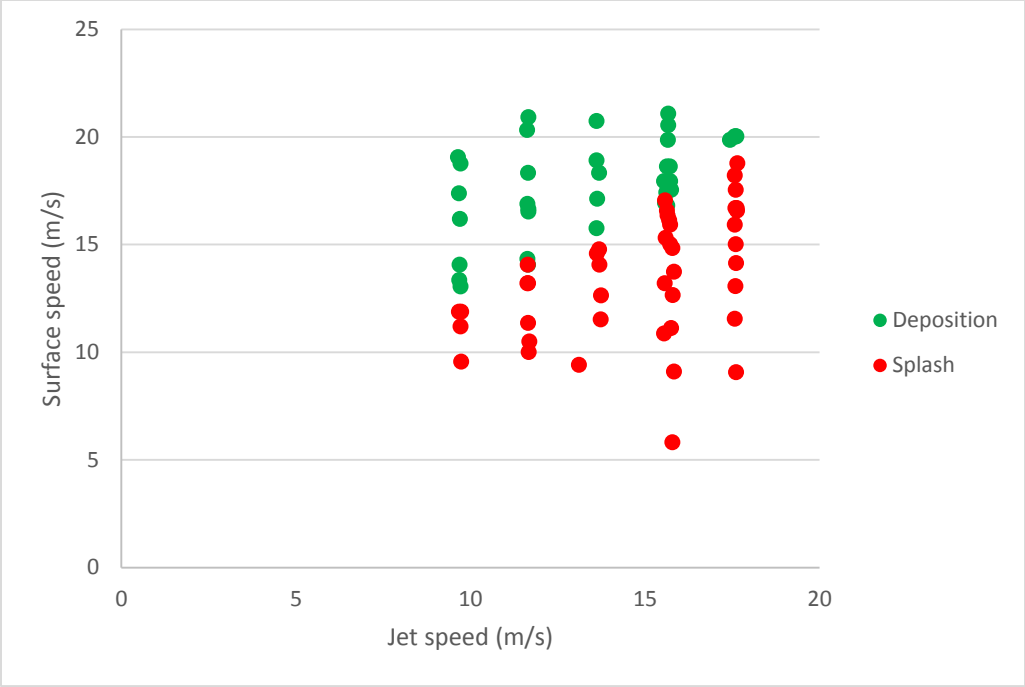

Figure 3-11 Simu liquid jet impingement on mirror surface test results

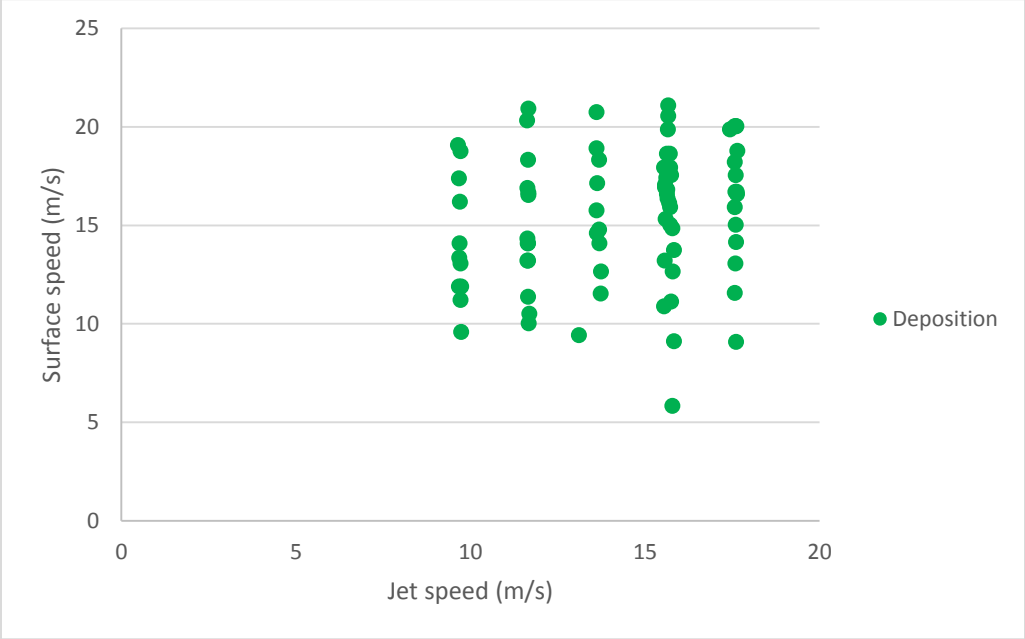

Figure 3-12 Simu liquid jet impingement on smooth surface test results

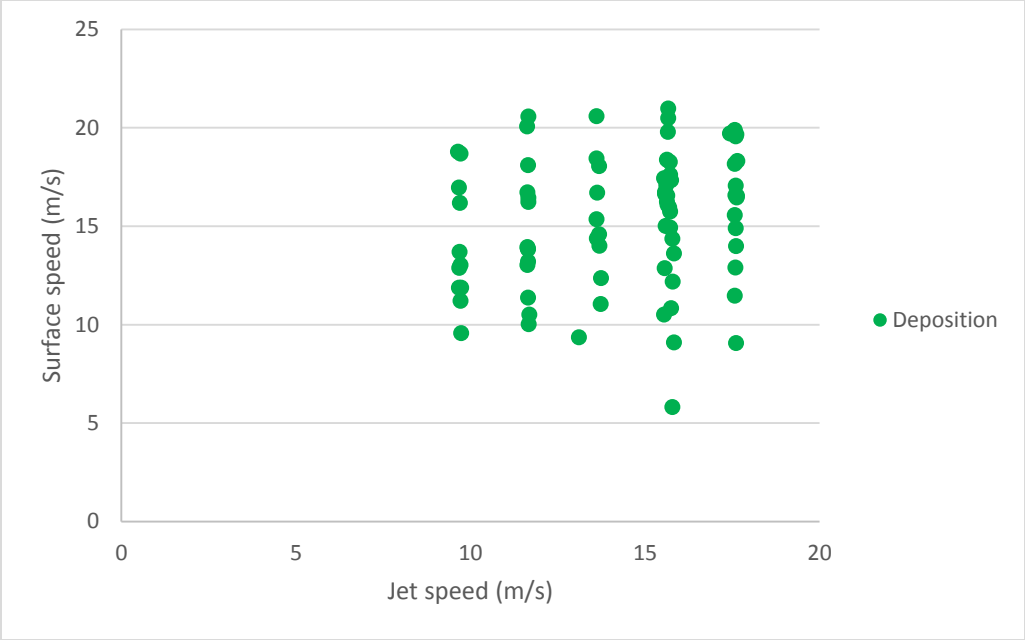

Figure 3-13 Simu liquid jet impingement on rough surface test results

3.2.2 Newtonian liquids

To further confirm the effects of surface roughness on liquid jet impingement, same experiments were also performed on the three surfaces with two Newtonian liquids: 70% glycerine-water solution (GW70) and 85% glycerine-water solution (GW85). Results are presented in Figure 3-14 to Figure 3-19.

With GW70, no deposition was achieved on the mirror surface due to extremely sensitive lamella. Any even tiny disturbance may trigger a splash. In a few rare cases where the jet seems to deposit on the surface at first, the deposition could not last for longer than 1 ms. GW85 shows stable deposition on all three surfaces.

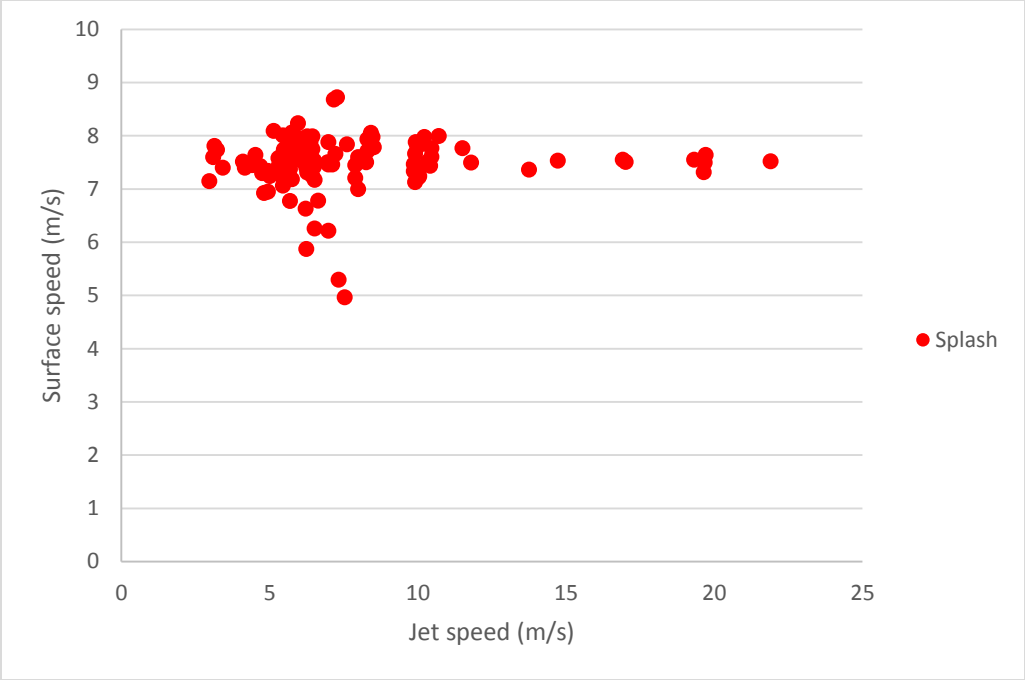

Figure 3-14 GW70 liquid jet impingement on mirror surface test results

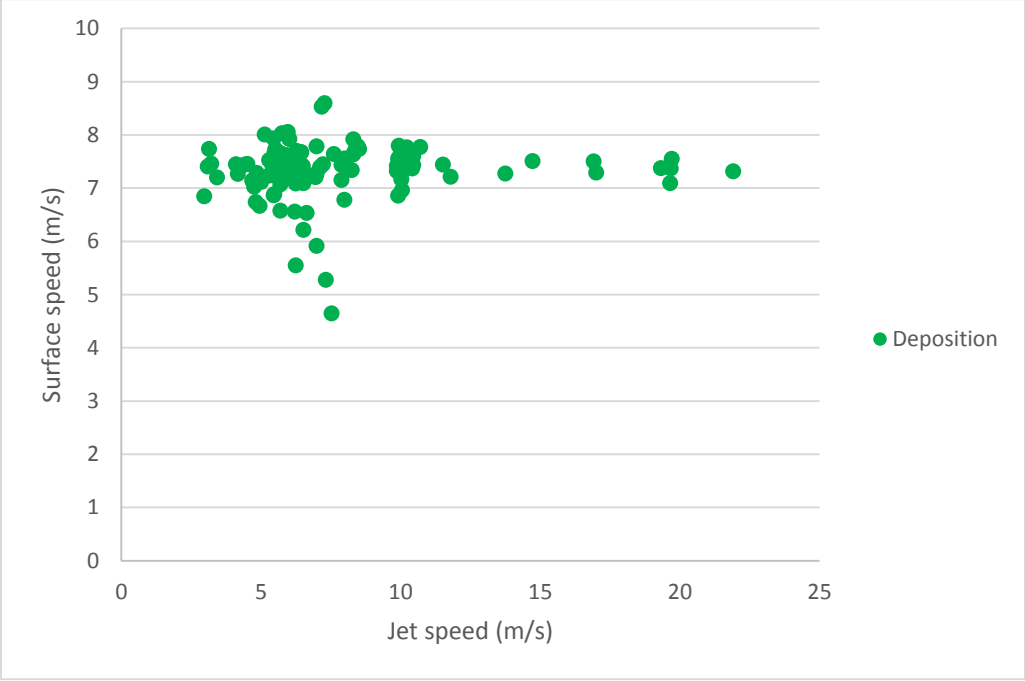

Figure 3-15 GW70 liquid jet impingement on smooth surface test results

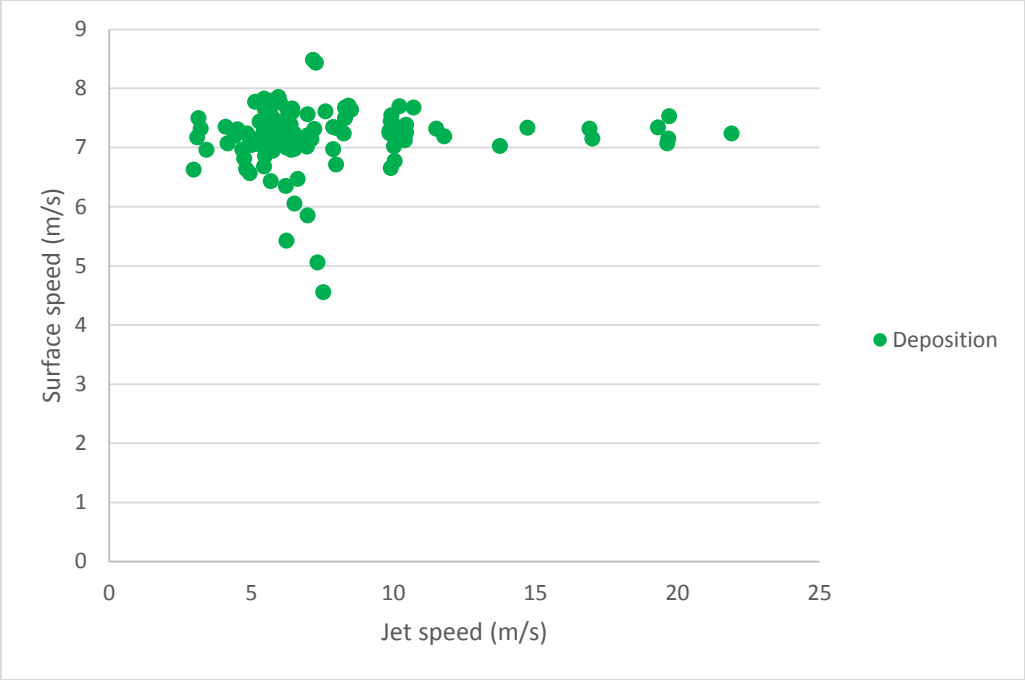

Figure 3-16 GW70 liquid jet impingement on rough surface test results

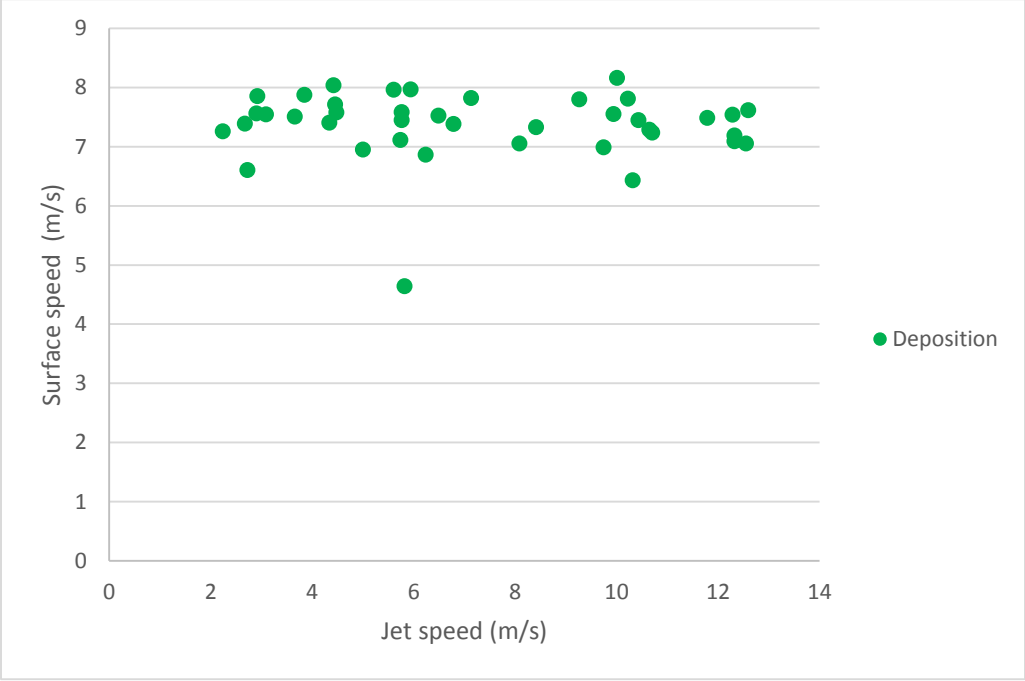

Figure 3-17 GW85 liquid jet impingement on mirror surface test results

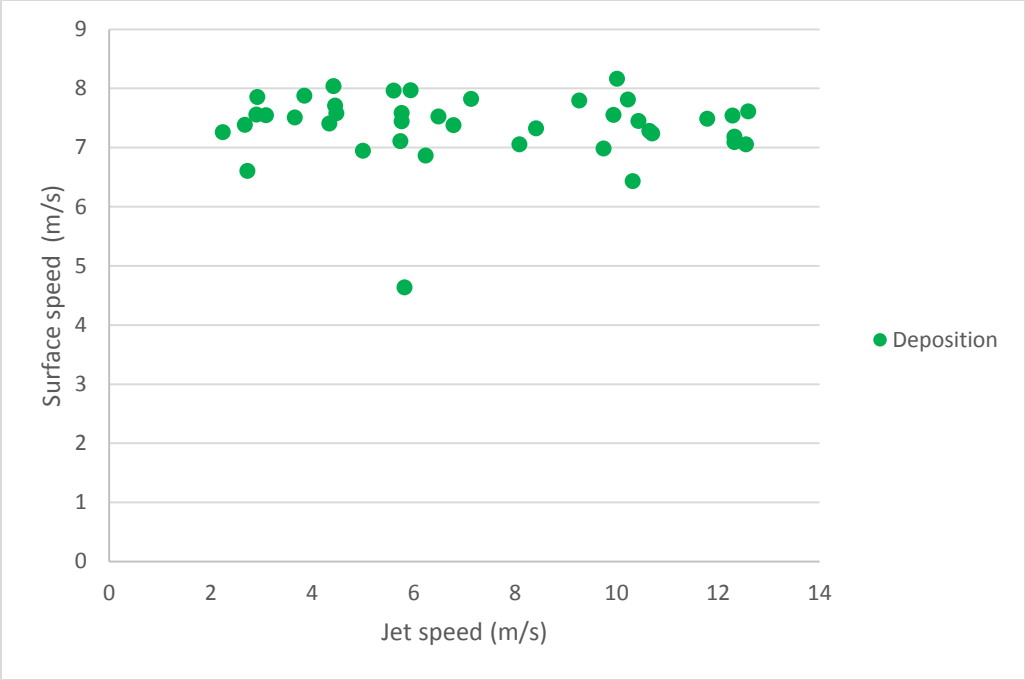

Figure 3-18 GW85 liquid jet impingement on smooth surface test results

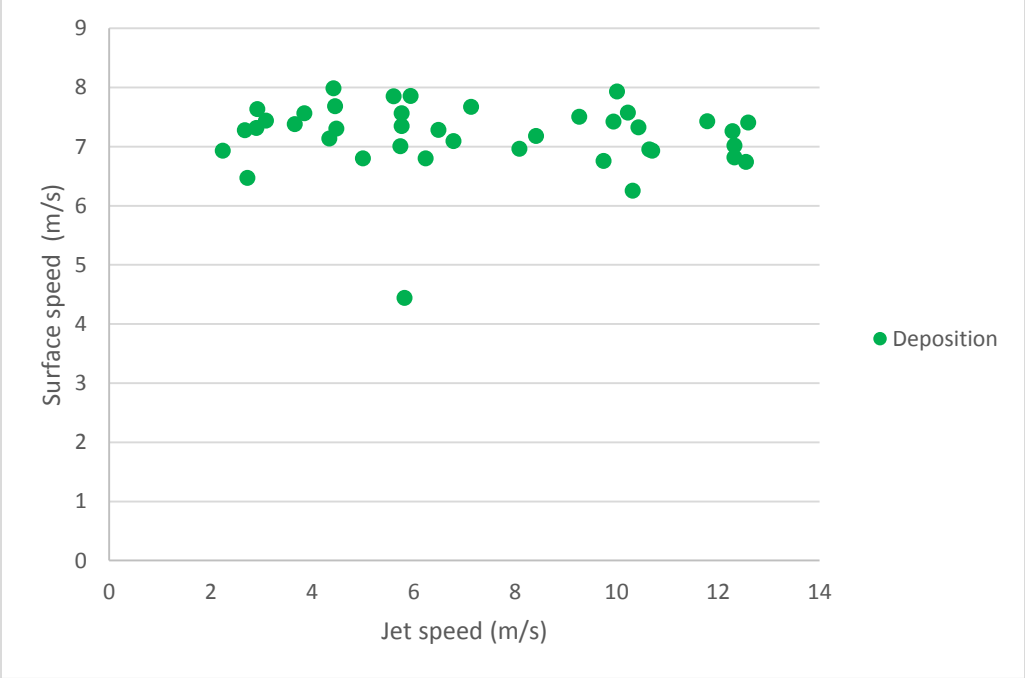

Figure 3-19 GW85 liquid jet impingement on rough surface test results

3.2.3 Effects of surface roughness summary

Table 3-4 summarizes test results of Newtonian liquids and LFMs. In these experiments, splash only occurred on the mirror surface (0.016 μm roughness height). On the two surfaces with slightly larger roughness (0.158 μm and 0.505 μm), no splash was observed, indicating that having small roughness on surface can suppress splash.

Table 3-4 Effects of surface roughness summary

Test liquid		Surface finish		
		Mirror	**Smooth**	**Rough**
Newtonian	**GW70**	Splash	Deposition	Deposition
	GW85	Deposition	Deposition	Deposition
LFMs	**AP2**	Splash/Deposition	Deposition	Deposition
	45oC	Splash/Deposition	Deposition	Deposition
	Simu	Splash/Deposition	Deposition	Deposition

3.2.4 Splash triggered by jet or surface imperfection

In some rare cases, the lamella of a liquid jet stream may interact with droplets or roughness on the surface in such a way that causes it to lift off from the impingement surface (Figure 3-20). In equally unusual circumstances, a small disturbance in the flow can produce irregularities in the jet, which upon surface impaction becomes amplified, causing the lamella to separate from the surface for a long period of time (Figure 3-21). These triggered splashes usually happen when doing experiments on the mirror surface since the lamella on the rougher surfaces has characteristics that permit it to better absorb such small disturbances.

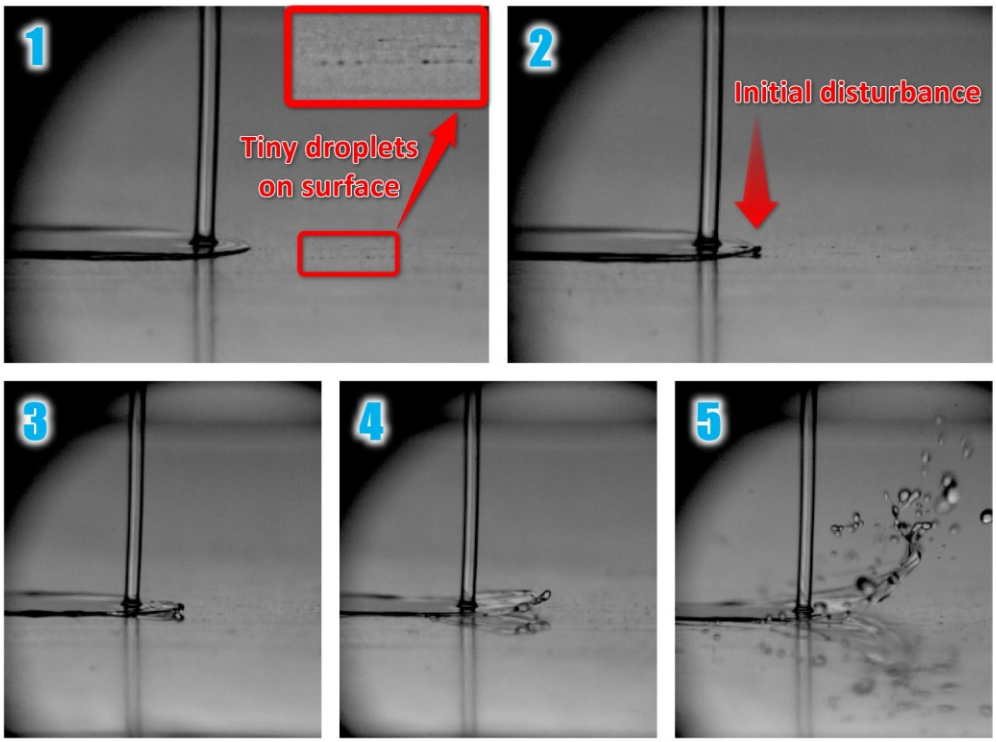

Figure 3-20 Time sequence showing the transition from jet deposition to jet splash. In this sequence the transition is caused by very fine droplets adhering to the otherwise dry substrate.

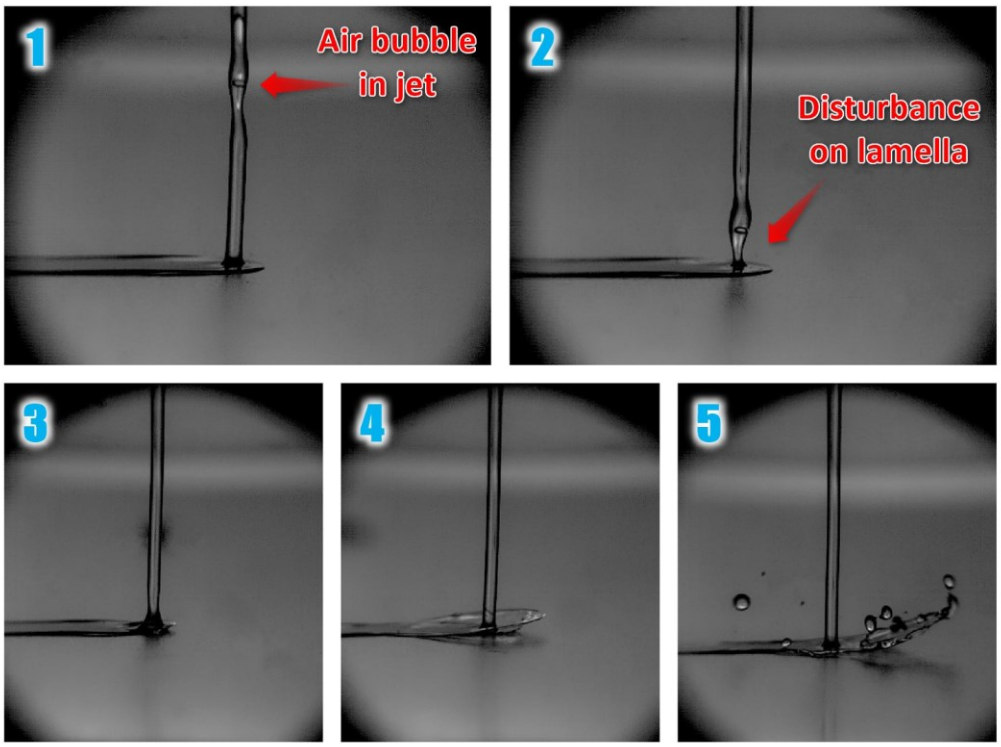

Figure 3-21 Time sequence showing the transition from jet deposition to jet splash. In this sequence the transition is caused by a small air bubble in the jet that perturbs the flow.

3.3 High speed commercial LFMs jet impingement test results

A series of experiments were conducted with commercial LFMs at high surface speeds to test the performance of the LFMs on high speed trains. The same 648 µm nozzle was used in these experiments. Surface speeds were varied between 15 m/s and 65 m/s, while jet speeds were varied between 8 m/s and 18 m/s. Average surface roughness height was 0.158 µm (smooth surface). Test results for Simu and AP2 are plotted in Figure 3-22 and Figure 3-23, respectively. In these tests, deposition occurred for every case without surface and jet disturbance.

Figure 3-22 Simu liquid jet high speed impingement test results

Figure 3-23 AP2 liquid jet high speed impingement test results

3.4 Jet and lamella dimensions

An extensive study on jet and lamella dimensions was performed for Newtonian and non-Newtonian liquids to better understand liquid jet impingement behaviours.

3.4.1 Newtonian liquids

For Newtonian liquids, a series of experiments were performed with four glycerine-water solutions of varying concentrations and four nozzles with different orifice diameters. Surface speeds were varied between 15 m/s and 65 m/s. Nozzle back pressures (NBP) were varied between 30 psig and 70 psig, giving jet speeds of 8 m/s to 25 m/s, depending on liquid viscosity and nozzle orifice size.

3.4.1.1 Lamella dimensions of interest

Three lamella dimensions were mainly studied for Newtonian liquids: lamella spread radius, *R*, lamella spread width, *W* and average lamella thickness, *h*. Of the three dimensions, lamella spread width and radius were measured directly from test images. Figure 3-24 depicts the lamella dimensions measurements.

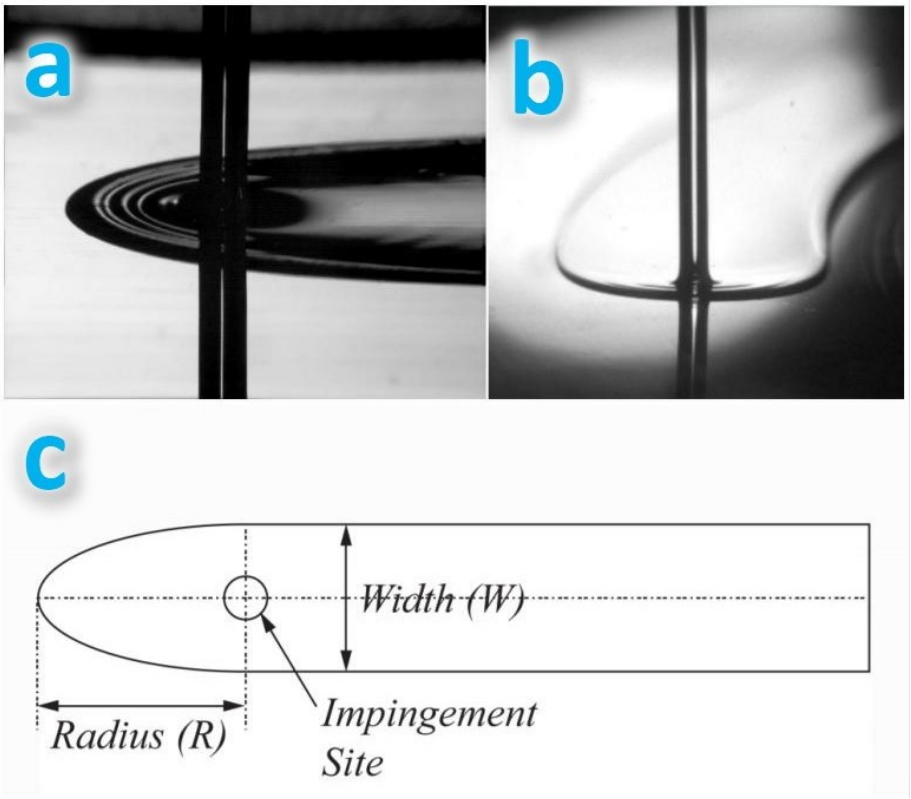

Figure 3-24 Lamella dimensions: a) lamella side view. b) lamella front view. c) lamella top view schematic

3.4.1.2 Lamella spread width and radius measurements

Lamella spread radius *R* and width *W* measurement results are shown in Figure 3-25 and Figure 3-26, respectively. Only results for 65% glycerine-water solution and 648 µm nozzle are presented in this section, but results for all four Newtonian liquids and four nozzles show the same trend. In these graphs, scatter points of same colour represent tests conducted at same

nozzle back pressure (± 1 psig). Jet diameter *D* is used as length scale for lamella spread radius and width. The error bars provided in these figures are calculated at a confidence level of 95%. The main source of the errors is the limited ability of the experimental set-up to keep test conditions strictly constant (e.g. slightly varying pressure, surrounding air flow field, vibrating surface, etc.).

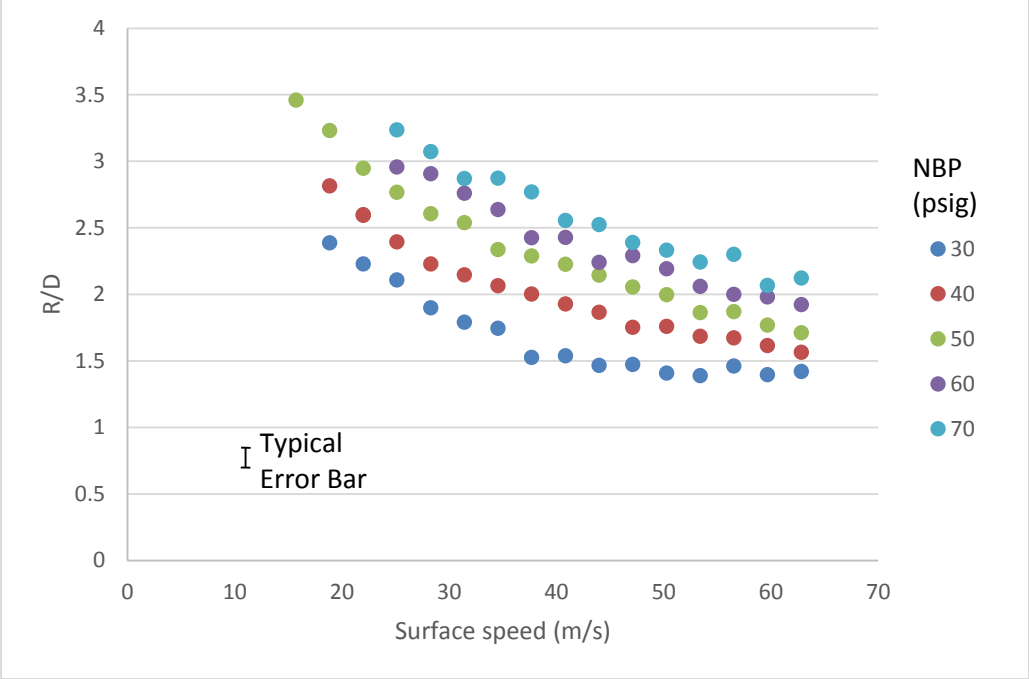

Figure 3-25 GW65 lamella spread radius measurements

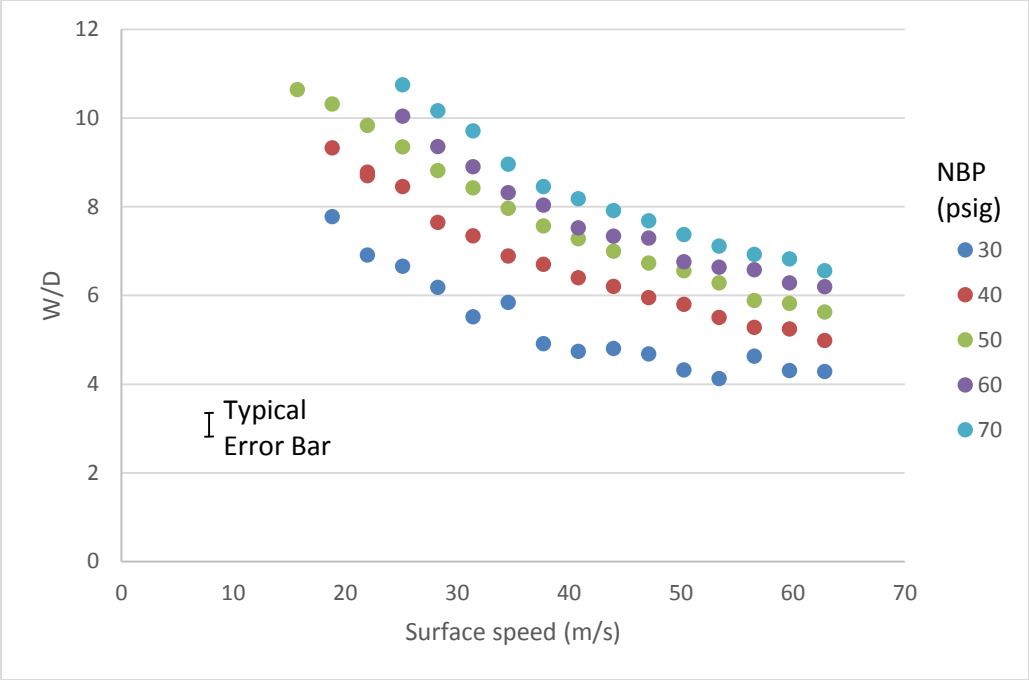

Figure 3-26 GW65 lamella spread width measurements

As shown in the two graphs above, lamella spread width and radius change with varying nozzle back pressure and surface speed in the same way: the two lamella dimensions decrease with increasing surface speed and decreasing nozzle back pressure (i.e. volumetric flow rate).

3.4.2 Non-Newtonian liquids

Four non-Newtonian liquids were tested on the spinning disk high speed test rig. Of the four non-Newtonian liquids, two are commercial LFMs and two are PEO-glycerine-water solutions.

3.4.2.1 AP2

AP2 lamella spread width and radius are shown in Figure 3-27 and Figure 3-28, respectively. The two dimensions change with nozzle back pressure and surface speed in the same way as Newtonian liquids.

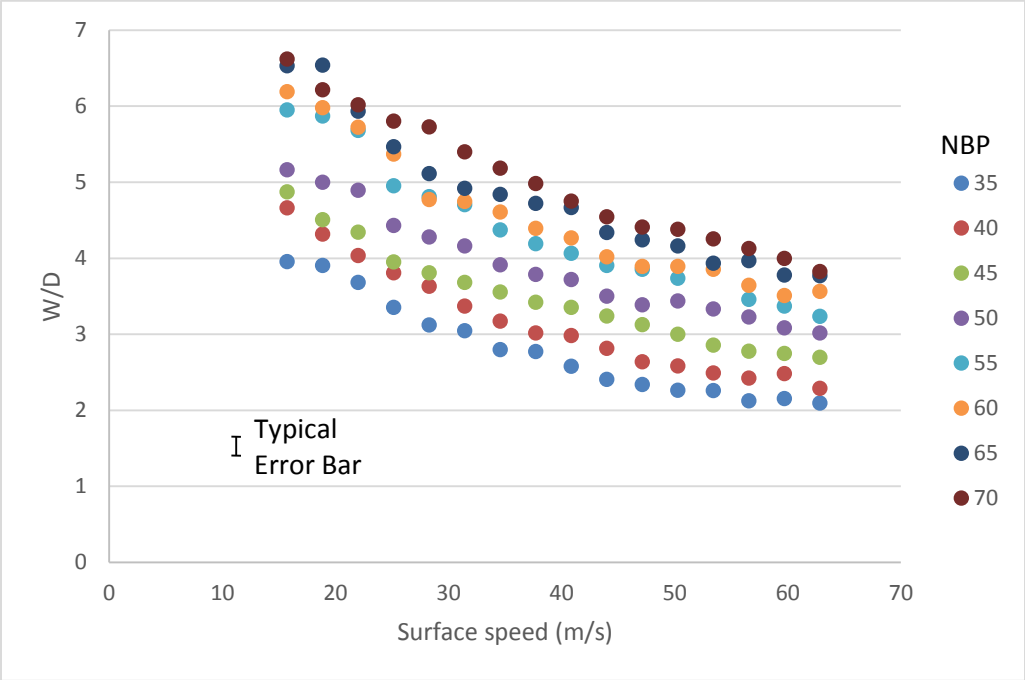

Figure 3-27 AP2 lamella spread width measurements

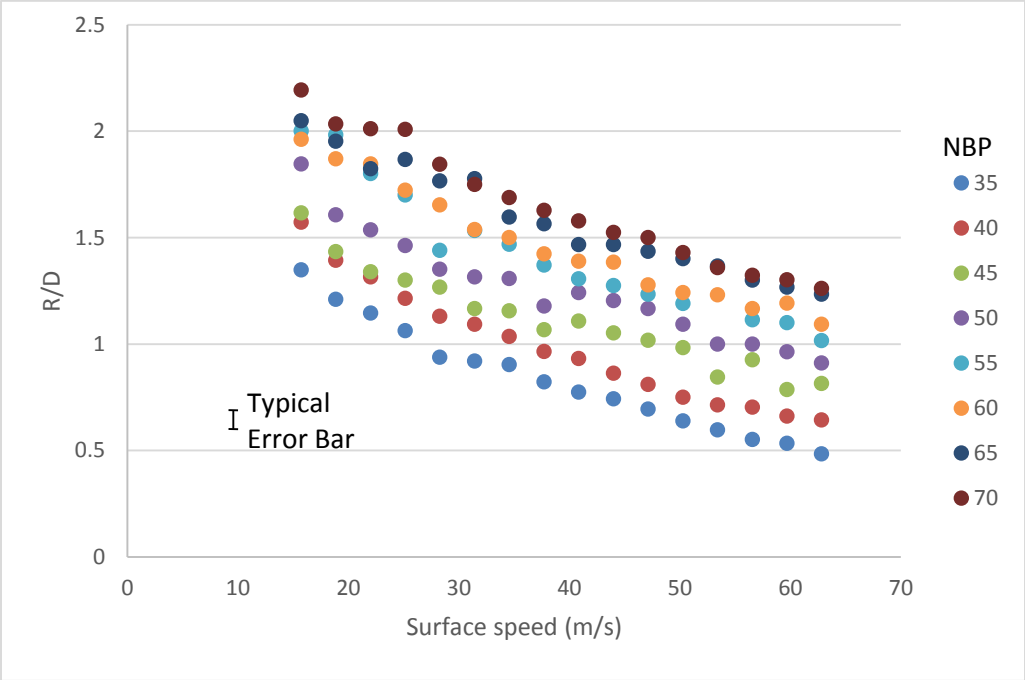

Figure 3-28 AP2 lamella spread radius measurements

Although lamella measurements show the same trend as Newtonian liquids, AP2 displays some non-Newtonian characteristics quite distinct from glycerine-water solutions. Figure 3-29 shows an example of AP2 jet impingement at low nozzle back pressure and high surface speed. Two distinct non-Newtonian behaviours are observed in the figure: jet necking and jet bending.

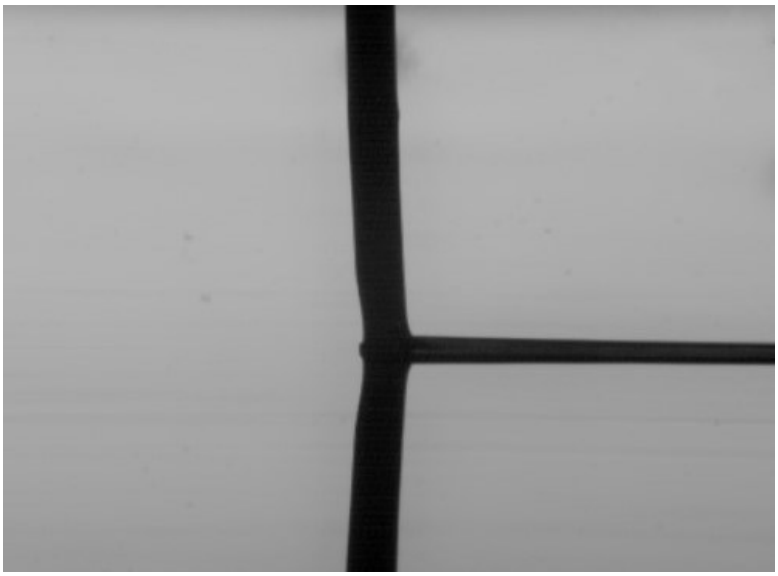

Figure 3-29 Non-Newtonian behaviours of AP2

Jet necking is the decrease of local jet diameter in the section right before the liquid jet impinges on the moving surface. As shown in Figure 3-29 and Figure 3-30, diameter of the liquid jet is smaller where it is close to the moving surface compared to upstream jet diameter. To study this local jet necking behaviour, jet necking ratio D_n/D is defined as the ratio of the smallest diameter of the jet in the section close to the moving surface to the free stream jet diameter upstream. Figure 3-31 plots the jet necking ratio measurements for AP2. As shown in the figure, jet necking only occurs at high surface speed and low nozzle back pressure. Necking ratio D_n/D increases with increasing surface speed and decreasing nozzle back pressure (or jet speed). Figure 3-30 illustrates the dimensions used in jet necking and jet bending measurements.

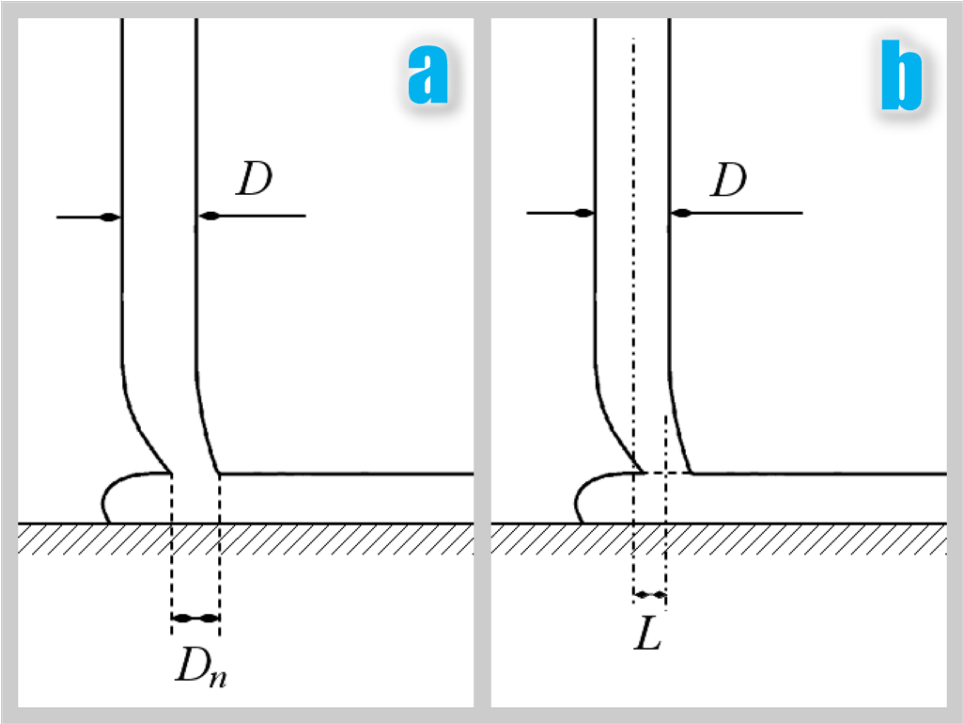

Figure 3-30 Schematic showing jet necking and bending dimensions.

a) **Dimensions for jet necking. b) Dimensions for jet bending.**

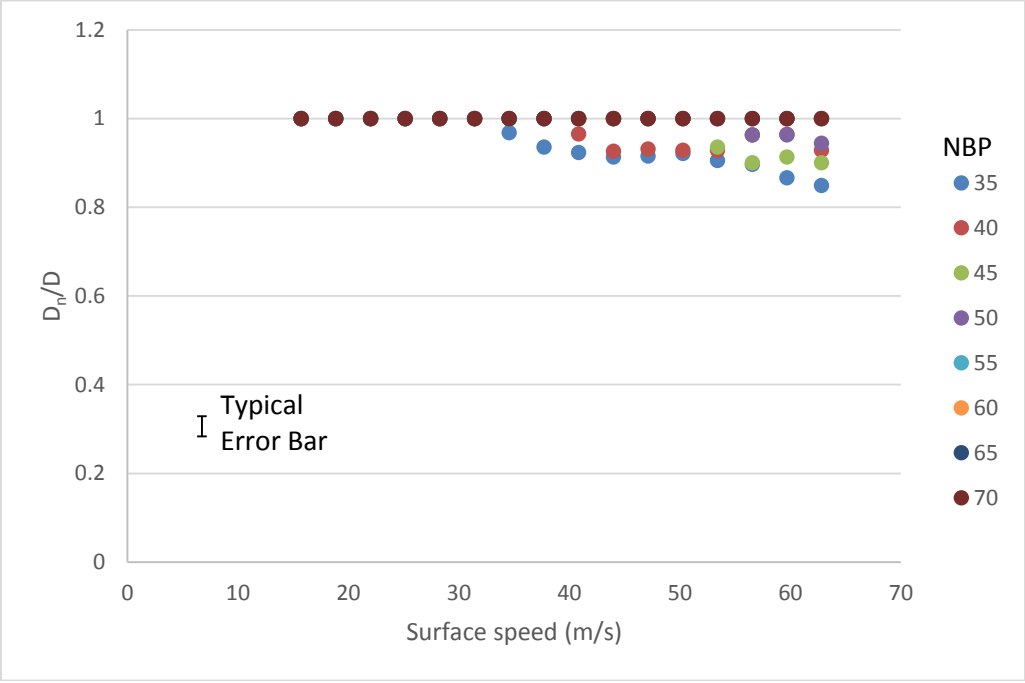

Figure 3-31 AP2 jet necking ratio D_n/D measurements

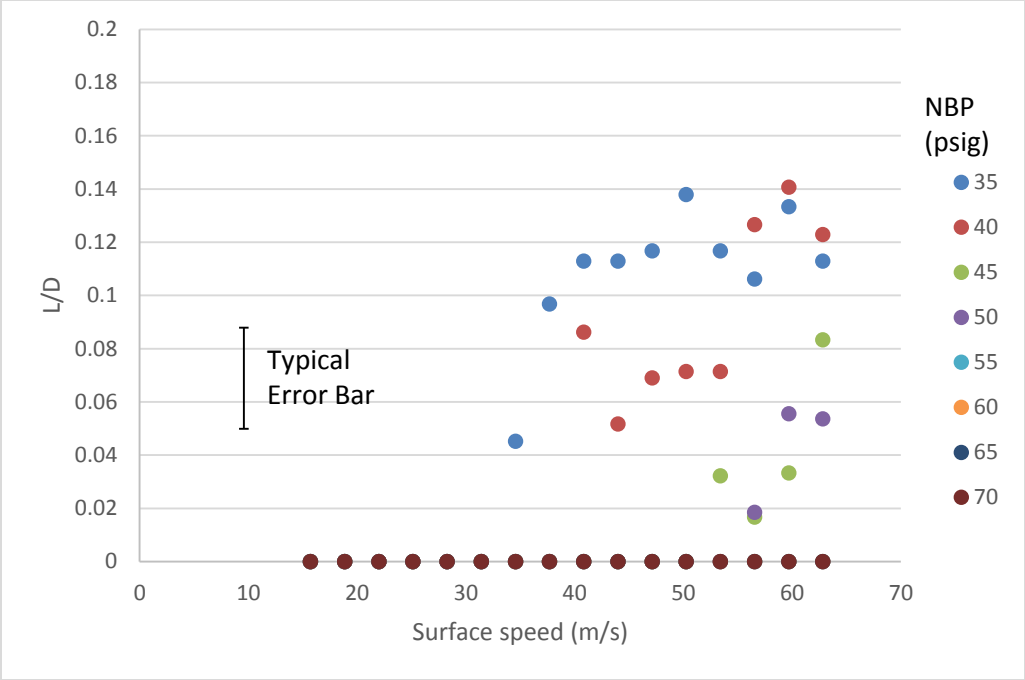

Figure 3-32 AP2 jet bending ratio L/D measurements

The jet bending behaviour observed here is the bending of the centerline of the liquid jet. Different from the bending of highly viscous Newtonian liquid jet [39], it is a non-Newtonian behaviour that only occurs in the region close to the moving surface. Jet bending length L is defined as the distance between the center of the impingement point and upstream jet centerline. Figure 3-32 plots the L/D ratio for AP2. As shown in the figure, jet bending only occurs at high surface speed and low nozzle back pressure. Bending ratio L/D increases with increasing surface speed and decreasing nozzle back pressure (or jet speed).

3.4.2.2 Simu

Figure 3-33 is an image of Simu liquid jet impingement at high surface speed and low jet speed. Compared to AP2, more aggressive local jet necking is observed in the figure. Figure 3-34 plots the necking ratio D_n/D measurements for Simu. Same as AP2, Simu jet necking only occurs at

high surface speed and low jet speed and the necking ratio increases with increasing surface speed and decreasing jet speed.

Figure 3-33 Non-Newtonian behaviour of Simu liquid jet

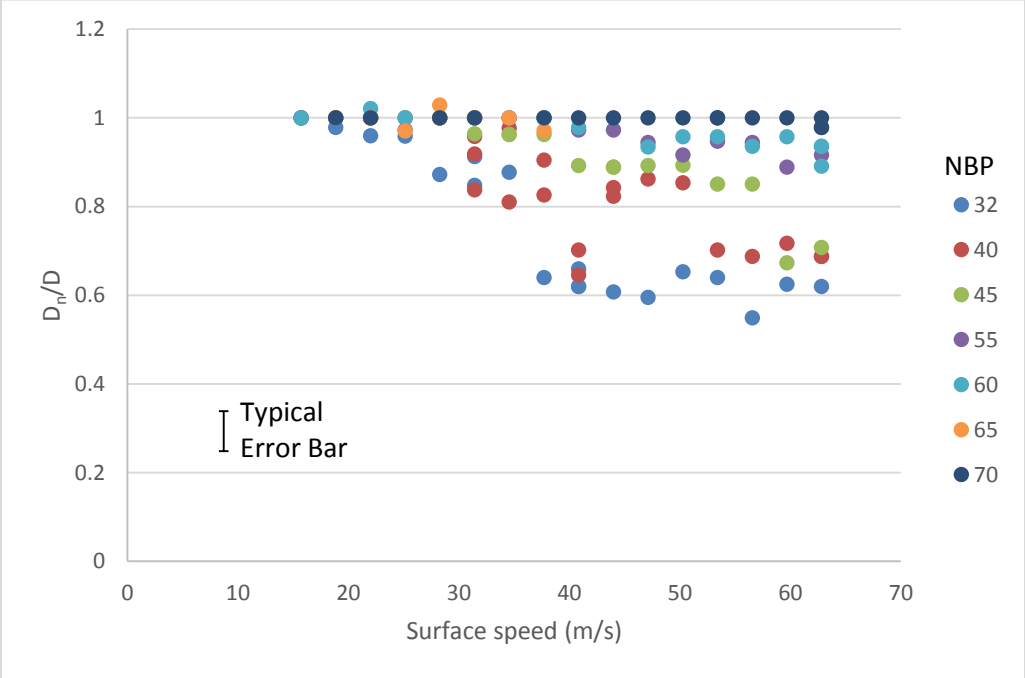

Figure 3-34 Simu jet necking ratio D_n/D measurements

3.4.2.3 PEO-glycerine-water solutions

Figure 3-35 is an image of PEO1000K liquid jet impingement side view. As shown in the image, a thin triangle liquid sheet forms behind the jet at the impingement point. This behaviour is likely a result of the normal stresses induced by the 'pulling' effect of the high speed moving surface on the jet.

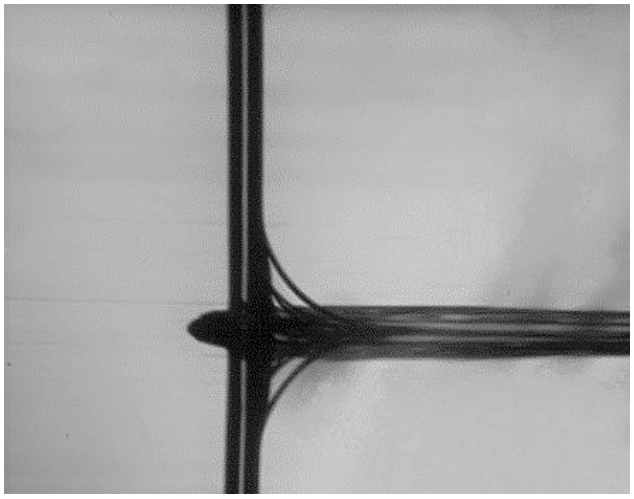

Figure 3-35 PEO1000K liquid jet impingement: jet stretching

Figure 3-36 is an image of PEO4000K liquid jet impingement. Compared to PEO1000K, the liquid sheet formed behind the jet is much larger due to increased elasticity. Front view of the jet impingement shows that the circular jet is stretched to a thin liquid sheet close to the surface.

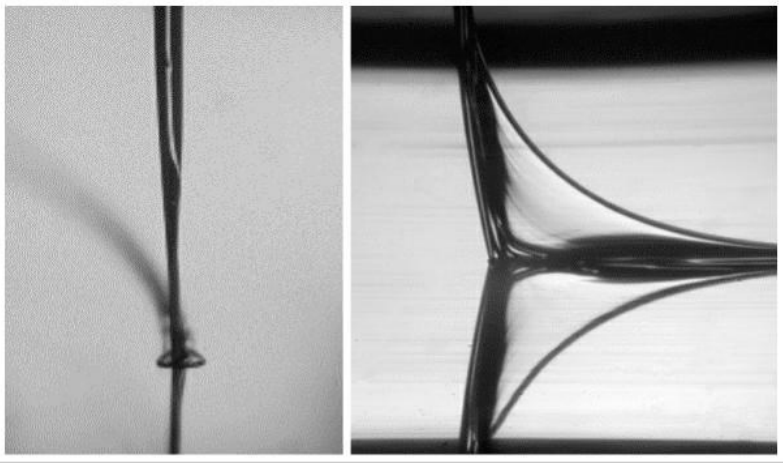

Figure 3-36 PEO4000K liquid jet impingement: jet stretching. Left: front view. Right: side view

Chapter 4: Analysis and Discussion

4.1 Lamella dimensions for Newtonian liquids

In this section, the measured lamella dimension results for Newtonian liquids are further analyzed. Two secondary lamella properties: average lamella thickness *h* and lamella shape ratio *W/R* are derived, and effects of liquid properties, jet properties and surface properties are studied.

4.1.1 Average lamella thickness *h*

With knowledge of lamella width *W*, volumetric flow rate *Q* and surface speed *Vs*, the average downstream lamella thickness *h* can be calculated using the continuity equation

$$h = \frac{Q}{W \cdot V_S} \qquad \textbf{Equation 4-1}$$

4.1.1.1 Average lamella thickness theory

Theoretical lamella thickness can be estimated by doing an order of magnitude analysis of Navier-Stokes equations in the lamella. This analysis is similar to that done by Prandtl in his analysis of the laminar boundary layer.

Continuity: $$\frac{\partial u}{\partial x} + \frac{\partial v}{\partial y} = 0$$

By balancing the two terms, we have $O(V_S/D) = O(v/h)$. Hence, the scale for vertical velocity is found to be $v = O(V_S h/D)$.

u - Momentum: $$u\frac{\partial u}{\partial x}+v\frac{\partial u}{\partial y}+\frac{1}{\rho}\frac{\partial p}{\partial x}=\nu\left[\frac{\partial^2 u}{\partial x^2}+\frac{\partial^2 u}{\partial y^2}\right]$$

The pressure gradient term can be immediately eliminated due to the presence of the free surface of the lamella. By considering the order of magnitude for each term in the u-momentum equation, we have

$$O\left(\frac{V_s^2}{D}\right)=O\left(\frac{\nu V_S}{h^2}\right)$$

Therefore,

$$h=O(\sqrt{\frac{\nu D}{V_S}}) \qquad \textbf{Equation 4-2}$$

Equation 4-2 states that thickness of the lamella is proportional to square root of liquid kinematic viscosity, liquid jet diameter and inversely proportional to square root of surface velocity.

4.1.1.2 Effects of jet speed and surface speed

Figure 4-1 plots the calculated average downstream lamella thickness *h*. As shown in the figure, the average lamella thickness is not a function of nozzle back pressure. Therefore, perhaps surprisingly, varying the volumetric flow rate (i.e, the jet velocity) has no discernible effect on the average lamella thickness. A simple least squares fitting was performed to find that average lamella thickness *h* is inversely proportional to square root of surface speed *Vs*. Therefore,

$$h=\frac{K}{\sqrt{V_S}} \qquad \textbf{Equation 4-3}$$

In **Equation 4-3**, K is constant for a certain fluid and nozzle combination.

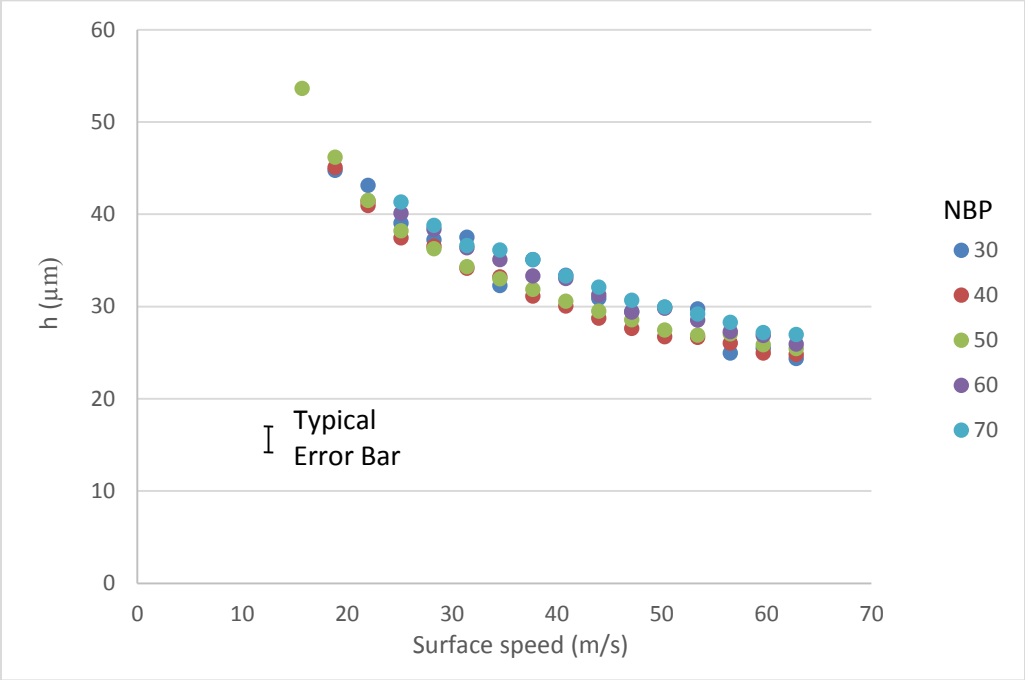

Figure 4-1 GW65 average lamella thickness

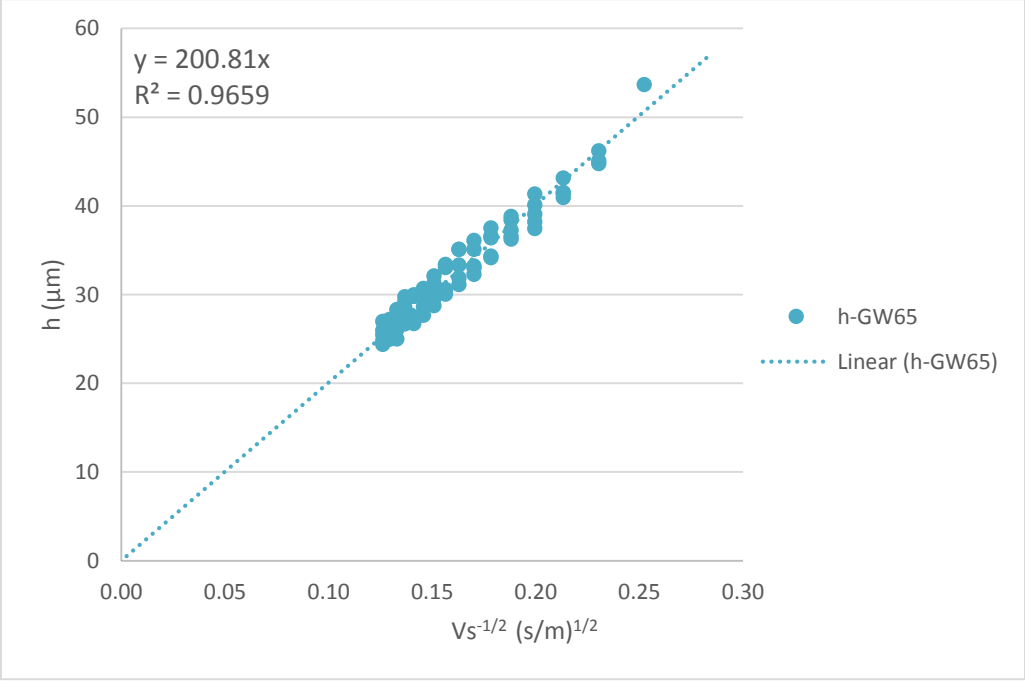

Figure 4-2 Average lamella thickness plotted against inverse of square root of surface speed

Figure 4-2 shows average lamella thickness plotted against inverse of square root of surface speed. Due to the inversely proportional relation describe in Equation 4-3, all data points in Figure 4-2 collapse well to a straight line that passes through origin. Although only results for GW65 and 648 µm nozzle are shown here, Equation 4-3 is also true for all the liquids and nozzles combinations tested. Figure 4-3 plots lamella thickness factor K in Equation 4-3 against liquid jet speed for 85% glycerine-water solution and 0.013" nozzle. The figure shows another example indicating that the thickness factor K is not a function of the jet speed.

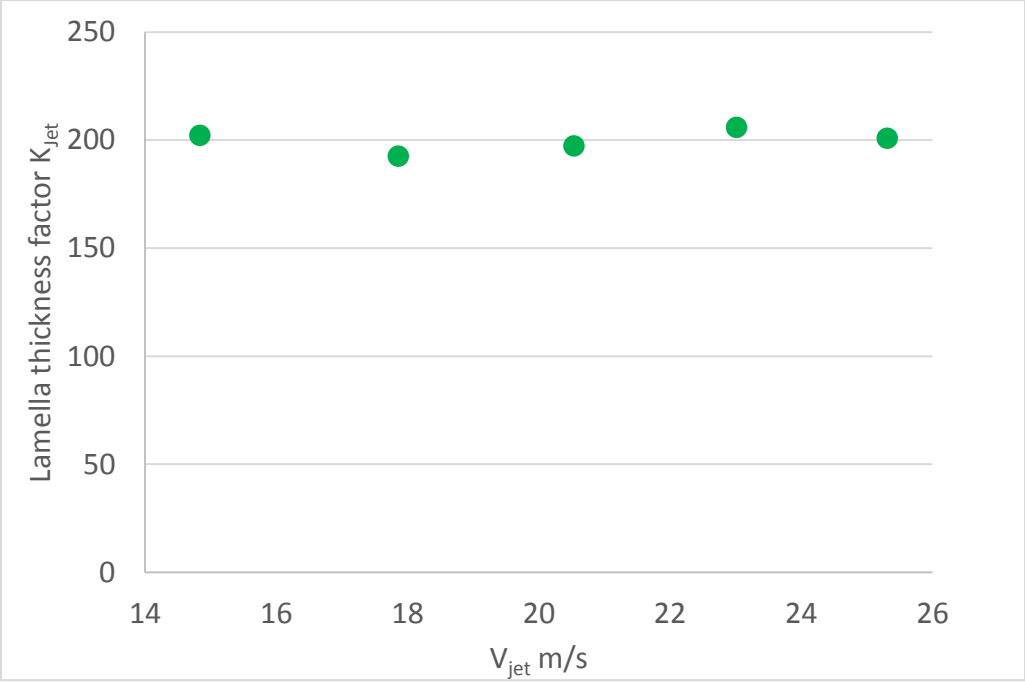

Figure 4-3 Lamella thickness factor against jet speed. Test condition: GW65/Nzl25

4.1.1.3 Effects of liquid viscosity

To determine the effects of liquid viscosity on average lamella thickness, three more glycerine-water solutions with different concentrations were tested. In these tests, the same 648 µm nozzle was used so that effects of nozzle orifice diameter are kept constant. Also, the effects of

volumetric flow rate and surface speed are known from Equation 4-3. Therefore average lamella thickness h can be written as

$$h = \frac{K_\nu}{\sqrt{V_S}} \qquad \textbf{Equation 4-4}$$

In which lamella thickness factor K_ν is only a function of liquid viscosity ν in these tests.

Figure 4-4 plots the lamella thickness factor K_ν against square root of liquid kinematic viscosity ν. The figure shows that lamella thickness factor K_ν is proportional to square root of liquid kinematic viscosity ν in these tests. Therefore Equation 4-3 becomes

$$h = K_D \sqrt{\frac{\nu}{V_S}} \qquad \textbf{Equation 4-5}$$

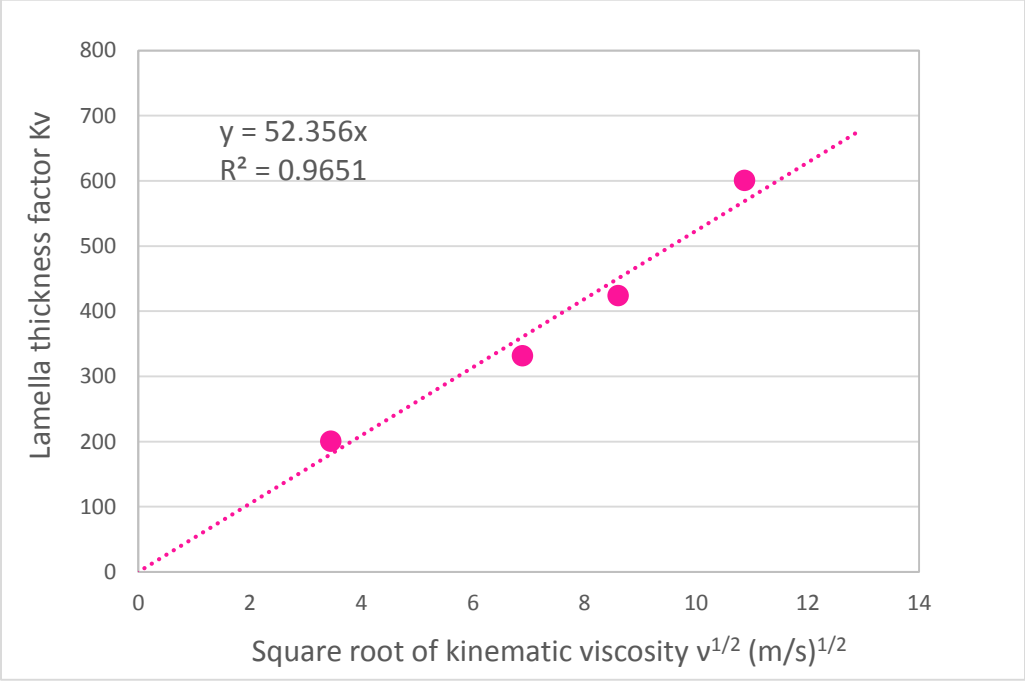

Figure 4-4 Effects of liquid kinematic viscosity on lamella thickness factor

4.1.1.4 Effects of liquid jet diameter

To determine the effects of liquid jet diameter on average lamella thickness h, four different nozzles with varying orifice sizes were tested. In these tests, only 85% glycerine-water solution was used so that the lamella thickness factor K in Equation 4-3 is only a function of liquid jet diameter D. Results are plotted in the form of lamella thickness factor K_D versus square root of jet diameter D in Equation 4-6. It can be seen from the figure that K_D is proportional to $D^{1/2}$. Therefore, combining Equation 4-5, Equation 4-3 finally becomes

$$h = K\sqrt{\frac{\nu \cdot D}{V_S}} \qquad \textbf{Equation 4-6}$$

In which K is not a function of volumetric flow rate, surface speed, liquid viscosity or liquid jet diameter, indicating that the experimental results match well with the theory (Equation 4-2).

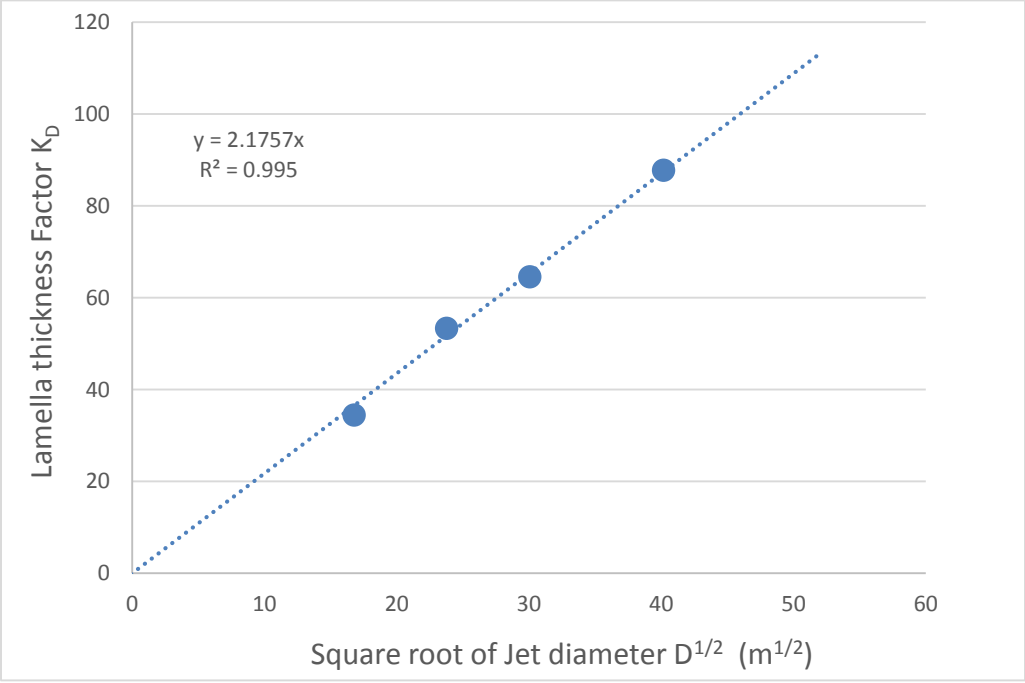

Figure 4-5 Effects of liquid jet diameter on lamella thickness factor

4.1.2 Lamella shape ratio W/R

Figure 4-6 plots lamella width/ lamella radius ratio for all surface speeds and volumetric flow rates. It can be seen from Figure 4-6 that the *W/R* ratio is almost constant for all test cases despite varying surface speeds and nozzle back pressures, indicating that, despite changing sizes, the planform shape of the lamella is almost constant for all test conditions. Although not shown here, this relation is also true for other Newtonian liquids and nozzles tested, and the *W/R* ratio is always a constant between 2.5 and 3.5.

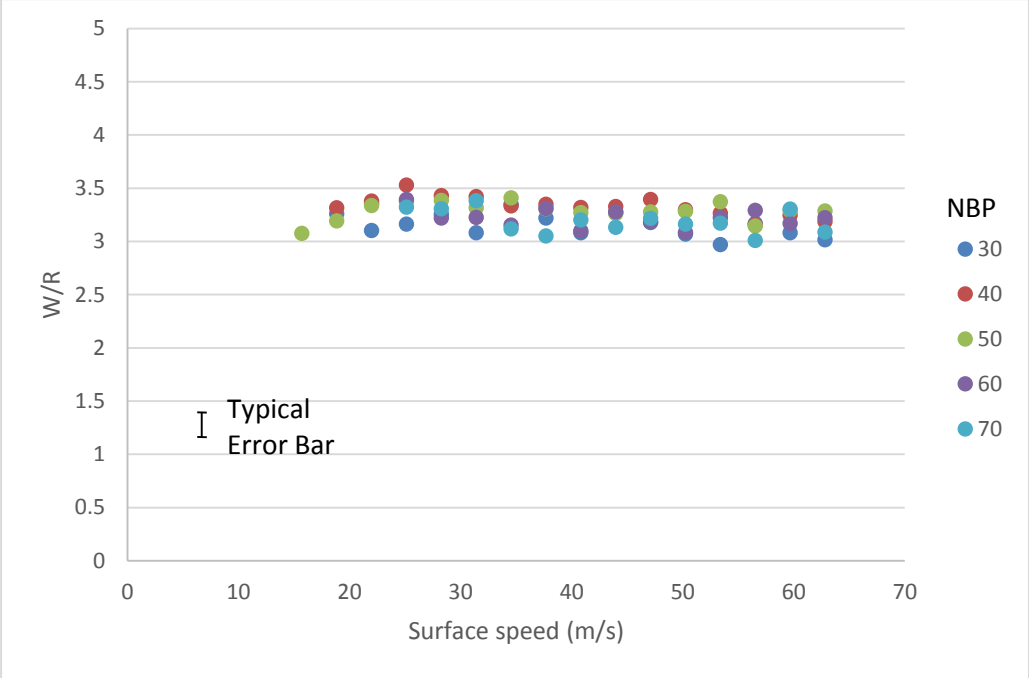

Figure 4-6 GW65 lamella spread width/radius ratio

4.1.3 Newtonian liquids lamella dimensions summary

To calculate the constant K in Equation 4-6, all the test results are plotted in a single graph in the form of h versus $x=(vD/V_s)^{1/2}$. Figure 4-7 shows the plot with more than 1,000 data points. In spite of varying volumetric flow rate, surface speed, liquid viscosity and liquid jet diameter, all data points collapse reasonably well onto a single line.

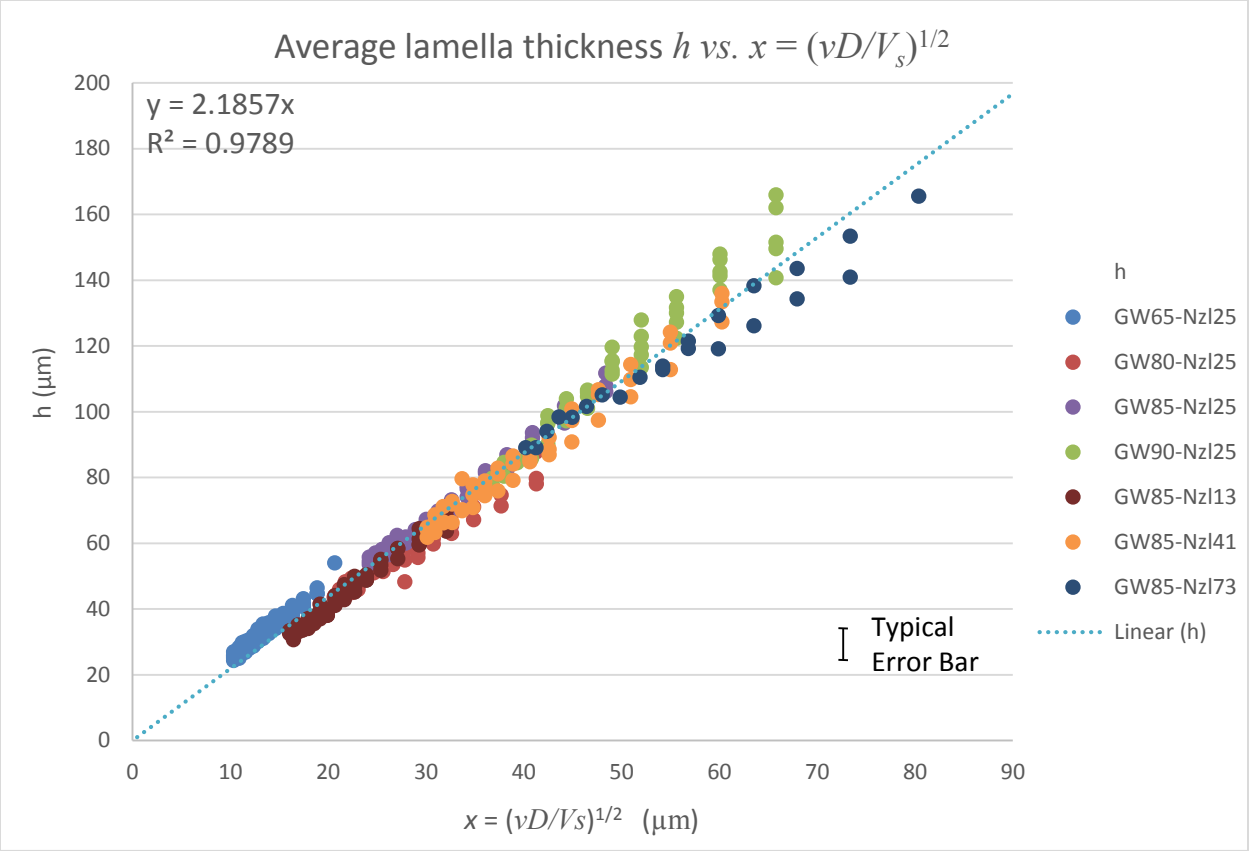

Figure 4-7 Average lamella thickness plotted against a combination of jet and surface properties

From a simple least square fitting, the constant K is found to be 2.1857. With previous results about spread radius R and width W, the following equations can be written to predict the lamella dimensions of interest (all variables in SI units).

$$\begin{cases} h = 2.186\sqrt{\dfrac{\nu \cdot D}{V_S}} \\ W = \dfrac{Q}{V_S \cdot h} \\ R \approx W/3 \end{cases}$$

Equation 4-7

With Equation 4-7, all three lamella dimensions of interest can be calculated without any experiments from known test conditions: liquid viscosity, jet diameter, surface speed and volumetric flow rate.

In Figure 4-7 the relevant length for scaling h was assumed to be the jet diameter (L_1 as defined in section 4.1.5 below). To determine if h could equally be scaled by the convective length scale of the flow, $L_2 = \sqrt{Q/V_s}$ (see section 4.1.5), Figure 4-7 was re-plotted using that length scale. The result is shown in Figure 4-8. As is immediately apparent, the data do not collapse nearly as well in this figure as in Figure 4-7, and therefore we conclude that the most salient scale for length is the jet diameter, D, not the convective length scale of the flow.

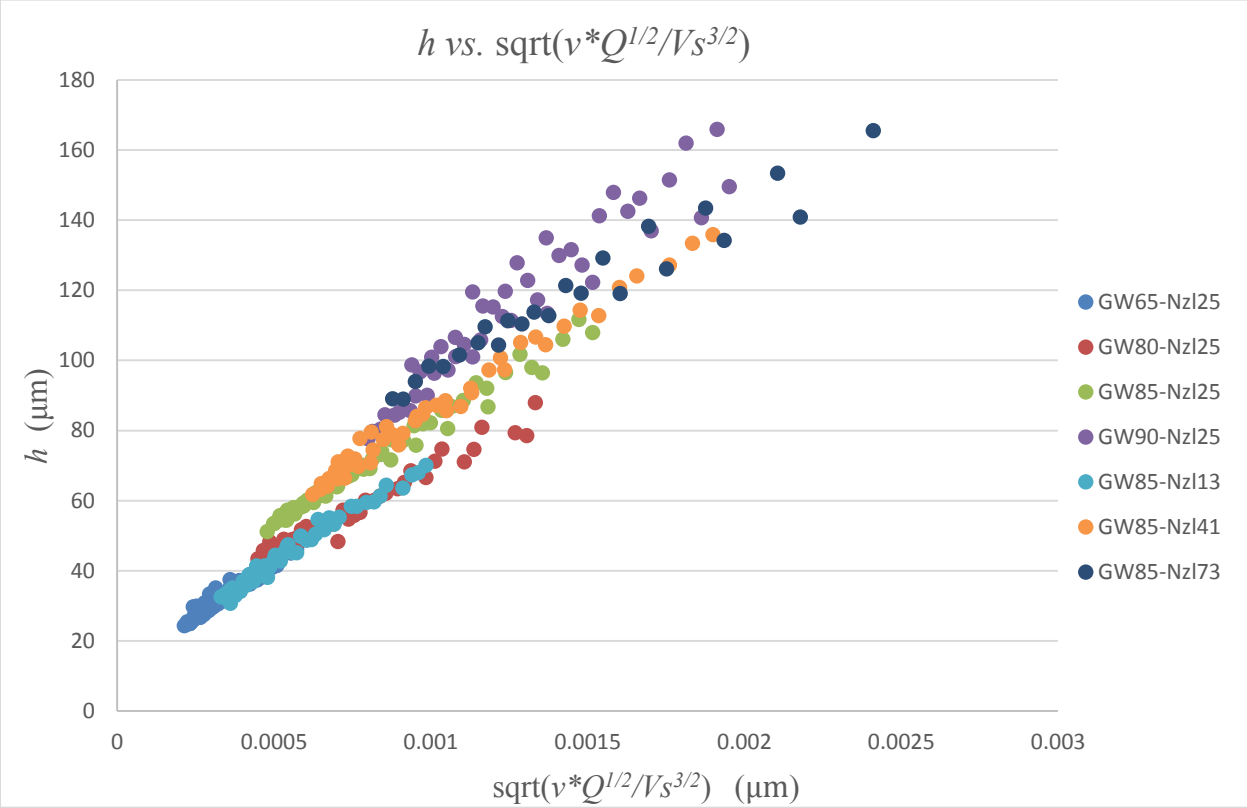

Figure 4-8 Average lamella thickness re-plotted using convective length scale

4.1.4 Newtonian liquids lamella dimensional analysis

It has been shown in the experimental results that the lamella spread dimensions are governed by the liquid jet diameter D, jet velocity V_{jet}, viscosity μ, density ρ, and the speed of the moving surface V_s. Although the surface tension, σ, is kept constant (±5%) in the Newtonian liquid experiments, it is included in this analysis for completeness. Surface roughness, though vital to splash characteristics, has been shown to have little effect on lamella spread dimensions and therefore is not explicitly considered. Hence, dependent variables in this problem (lamella dimensions) can be written in the form of

$$L = f(D, \mu, \rho, V_{Jet}, V_S, \sigma) \qquad \textbf{Equation 4-8}$$

L being one of the lamella dimensions. Following the Buckingham pi theorem [40], Equation 4-8 can be re-expressed in terms of four dimensionless groups. One way to group the variables is

$$\Pi_1 = \frac{L}{D}$$

$$\Pi_2 = \frac{\rho V_{jet} D}{\mu} = Re_{jet}$$

$$\Pi_3 = \frac{\rho V_S D}{\mu} = Re_s \qquad \textbf{Equation 4-9}$$

$$\Pi_4 = \frac{\rho {V_S}^2 D}{\sigma} = We$$

Hence, Equation 4-8 becomes,

$$L/D = \overline{f}(Re_{jet}, Re_S, We) \qquad \textbf{Equation 4-10}$$

With Equation 4-10 in mind, function $\overline{f}$ is determined by varying Re_{jet} and Re_S separately for each lamella dimensions, yielding results plotted in Figure 4-9, Figure 4-10 and Figure 4-11. The substantial collapse of the data in all three graphs implies that the complicated impingement physics involving 7 variables are well represented by a comparatively simple model with only two or three variables. Figure 4-11 is evidence that the average non-dimensional lamella thickness is governed only by the surface Reynolds number. Once this constraint is established, mass conservation then requires the linear dependence of *R/D* and *W/D* on the jet Reynolds number.

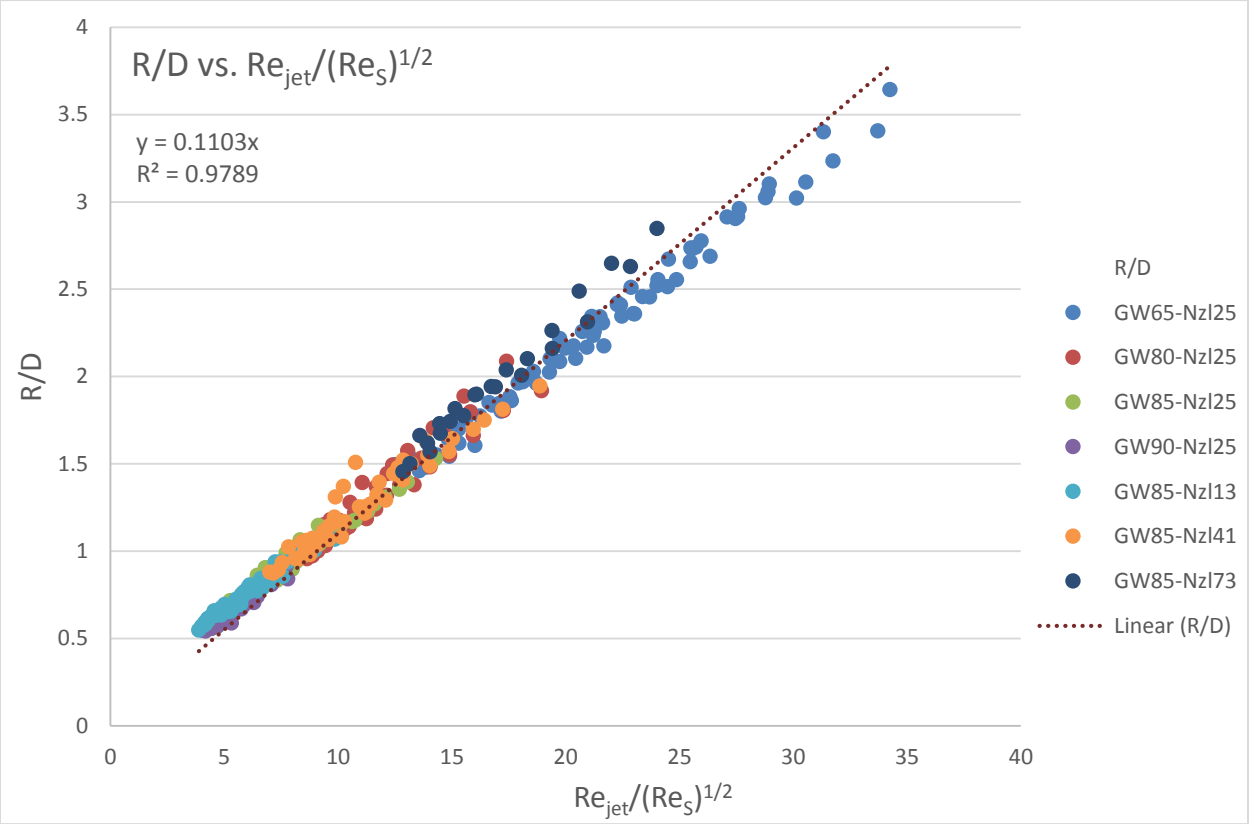

Figure 4-9 Dimensionless lamella spread radius R/D

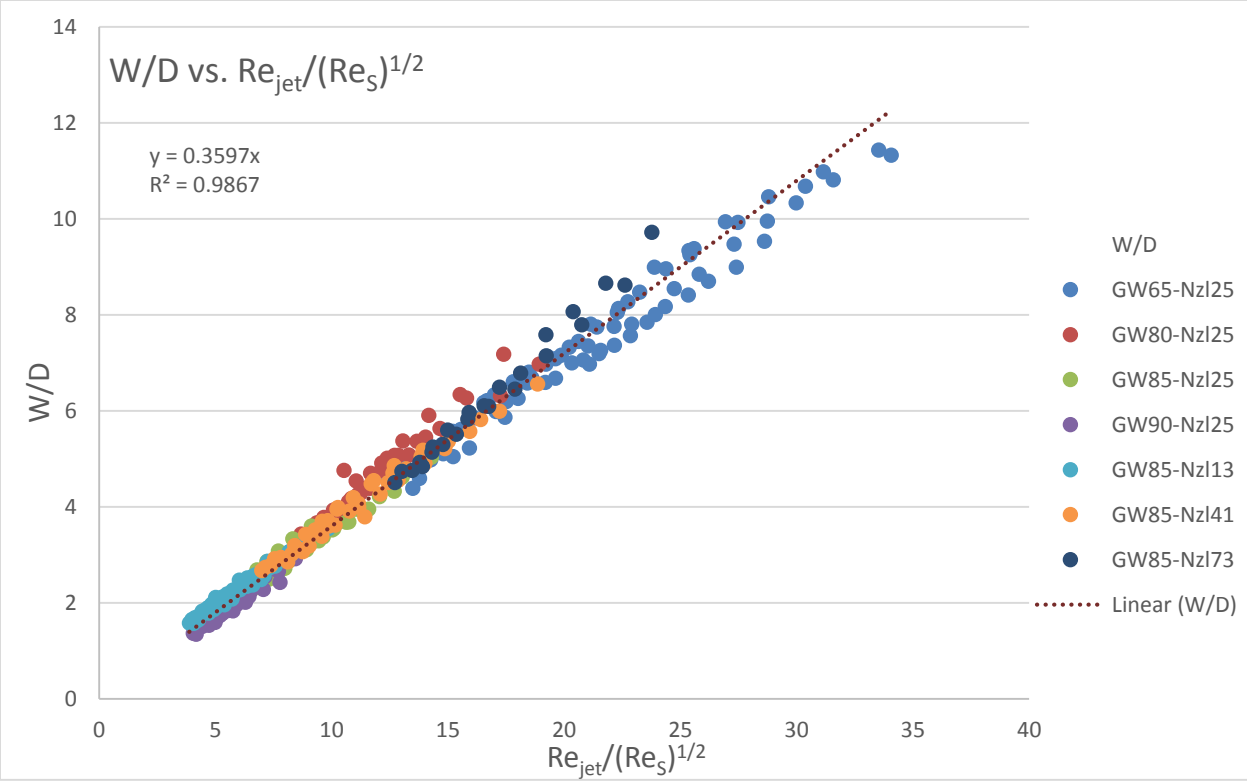

Figure 4-10 Dimensionless lamella spread width W/D

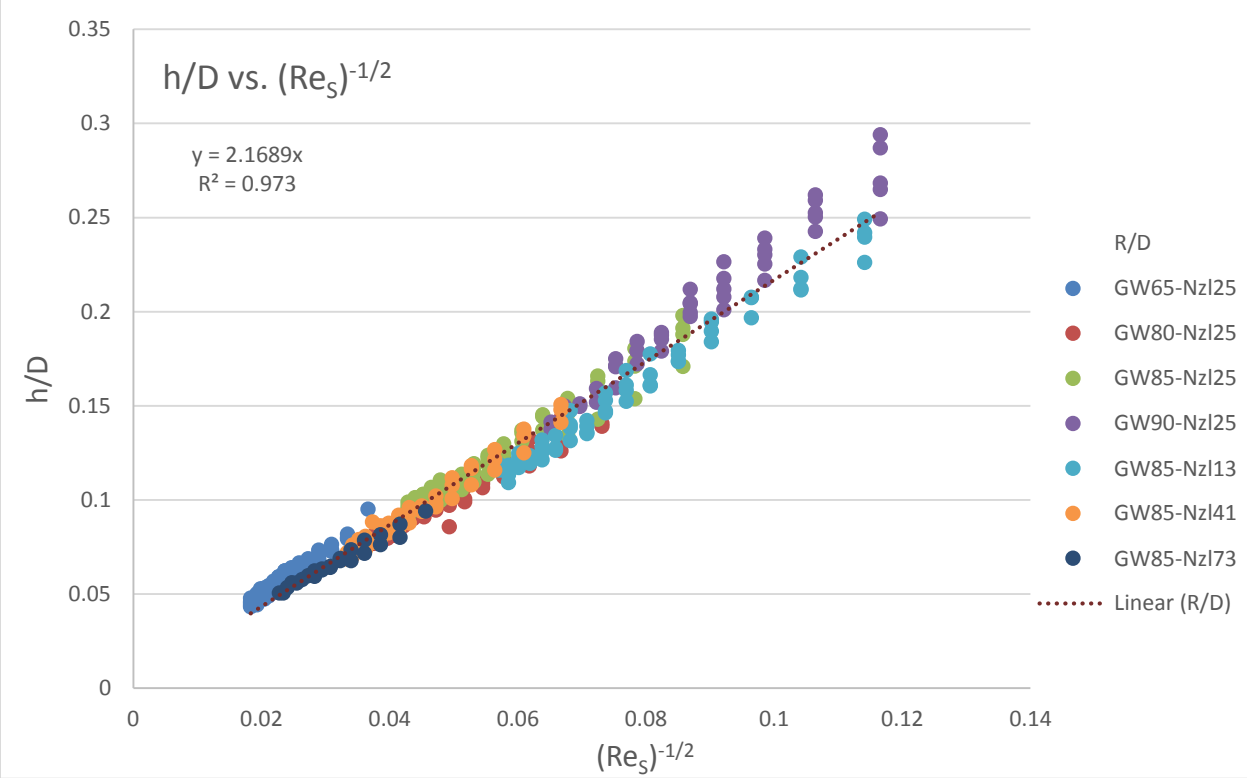

Figure 4-11 Dimensionless lamella average thickness h/D

In reference to Figure 4-9 it is interesting to observe that the curves collapse for R/D values as small as 0.5. R/D=0.5 (see Figure 3-24) corresponds to a flow with absolutely no lamella at all, and even R/D values up to 1.0 represent flows with extremely small lamella. One would not anticipate that such flows, with highly curved lamella streamlines, would have the characteristics predicted by the simple analysis presented in 4.1.1.1.

4.1.5 Newtonian liquids lamella dimensions theory

Four length scales were initially identified in the lamella spread dimensions problem,

- Natural length scale, liquid jet diameter $L_1 = D$
- Convective length scale $L_2 = \sqrt{Q/V_S}$, with Q being volumetric flow rate of the jet
- Viscous length scale $L_3 = \mu/\rho V_S$
- Capillary length scale $L_4 = \sigma/(\rho V_s^2)$

However, both the dimensionless analysis and constant *W/R* ratio indicate that there is only one dominant length scale in this problem. The proposed explanations for this are as follows.

1) $L_2 = \sqrt{Q/V_S} = \sqrt{\pi/4} \cdot \sqrt{V_{jet}/V_S} \cdot D$, which is the same order of magnitude as D. We do not know why the data collapses well when scaled by L_1 and not by L_2.
2) A typical value of L_3 is on the order of 10^{-6}m, which is three orders of magnitude smaller than typical values of D, which is on the order of 10^{-3}m, and L_3 is therefore not believed to be important.
3) A typical value of L_4 is also on the order of 10^{-6}m and is therefore not believed to be important in scaling the lamella overall dimensions.

4.2 Jet and lamella dimensions for non-Newtonian liquids

Jet and lamella measurement results for non-Newtonian liquids are analyzed and discussed in this section. Attempts to explain the results are made.

4.2.1 Lamella dimensions

Figure 4-12 plots the lamella width/radius ratio. Same as the ratio for Newtonian liquids, the *W/R* ratio for AP2 is also a constant around 3.

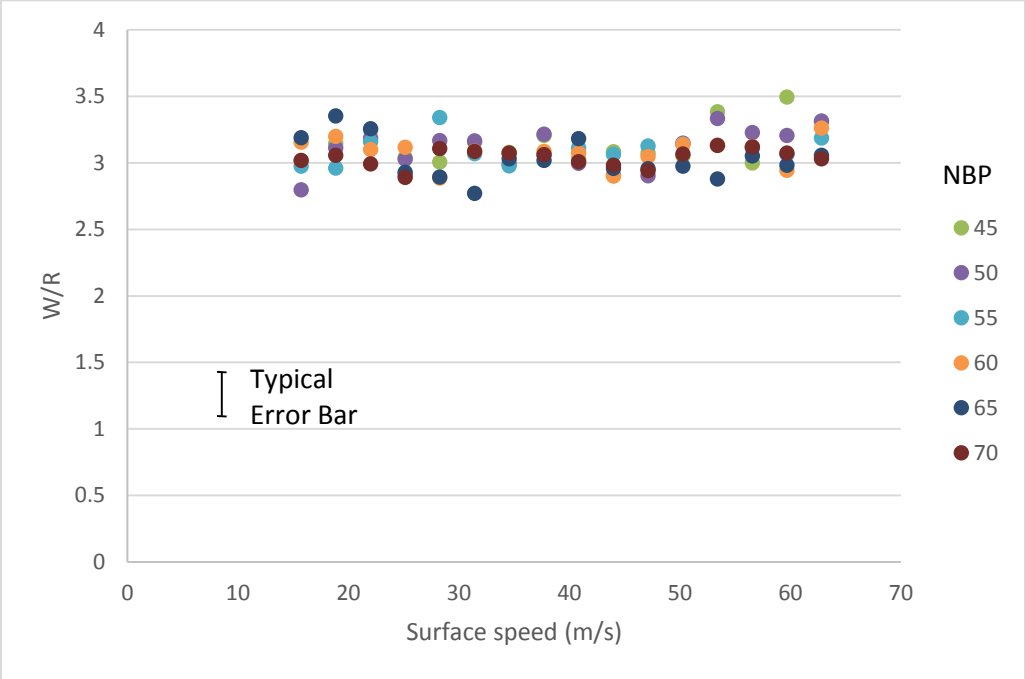

Figure 4-12 AP2 lamella spread width/radius ratio

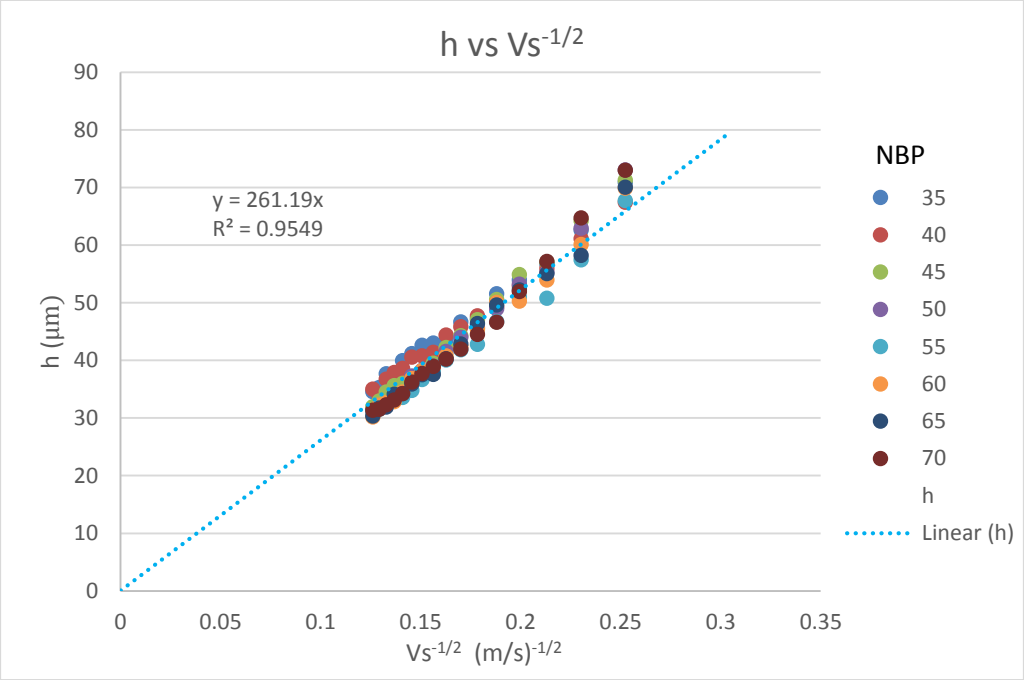

Figure 4-13 AP2 average downstream lamella thickness

With knowledge of lamella width W, volumetric flow rate Q and surface speed Vs, average lamella thickness h can be calculated as $h=Q/(W*Vs)$. Figure 4-13 shows that AP2 average lamella thickness h is also inversely proportional to square root of surface speed and independent of volumetric flow rate.

4.2.2 Jet behaviours

The three unique jet behaviours: jet necking, jet bending and jet stretching were never observed for non-Newtonian liquids. By comparing liquid properties of PEO1000K and PEO4000K solutions with GW65 and GW70 solutions (Table 2-1), it is evident that jet stretching results from liquid elasticity.

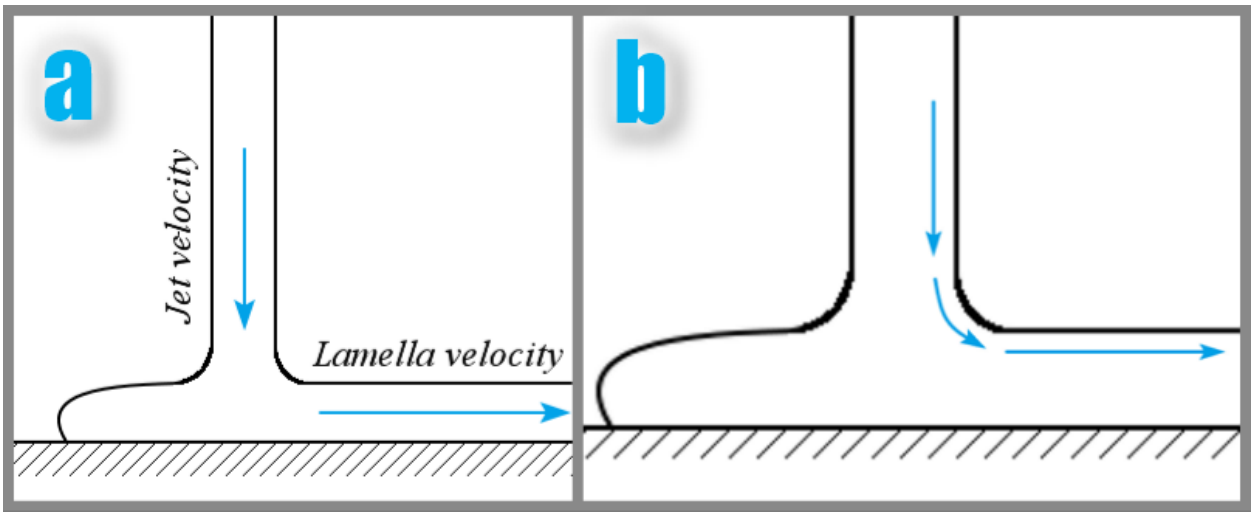

Figure 4-14 Bending of streamline near impingement point

Figure 4-14 shows a schematic of jet impingement. Due to the nature of liquid flow, the liquid streamline bends around the corner where the jet meets the lamella, resulting in a fillet shaped corner instead of a sharp one. Since in the impingement experiments, both the jet and surface move at high speeds, perturbations coming from fluctuating nozzle back pressure, surrounding air flow and surface imperfections pass through the rounded corner frequently. While for Newtonian liquids, such perturbations are suppressed by surface tension force, for elastic liquids, they are sustained by tension in fluid streamlines. Therefore, a liquid sheet may form and grow in size behind the jet in the direction of surface motion. The nearly triangular shape of the liquid sheet provides a smooth path for the flow to change its direction. The size and shape of the liquid sheet are dependent on lamella speed, inertia of the liquid jet and elasticity of the test liquid.

Simu and AP2 are non-Newtonian liquids with higher viscosity and elasticity, thereby exhibiting behaviours closer to solids than dilute aqueous PEO-glycerine solutions. The decreased jet diameter before impacting the surface indicates an increased liquid jet velocity in the region. This increase in liquid velocity is caused by the difference between surface speed and jet speed.

After impacting the surface, liquid deposited on the surface (the ‘lamella’) is accelerated to surface speed almost instantaneously due to its high viscosity. This difference in liquid velocity induces tension in streamlines due to elastic liquid’s resistance to extensional flow, therefore accelerates the liquid jet in the same way Fano flow defies gravity (‘open syphon’ flow). This theory is supported by the fact that jet necking only happens when surface speed is larger than jet speed and is most evident when surface speed is significantly larger than jet speed. Jet bending can also be explained in the same way as jet stretching and necking.

Chapter 5: Conclusions and Recommendations

5.1 Conclusions for effect of surface roughness on splash characteristic

An experimental investigation into the effect of small surface roughness on liquid jet impingement on a moving surface was performed. The study was carried out with both Newtonian and non-Newtonian liquids impacting dry surfaces with roughness heights ranging from 0.01 to 0.6 μm. A variety of jet speeds, surface speeds and liquid properties were used in this study. The interaction between the impinging jet and the moving surface was observed through high-speed imaging. The key findings of this study are:

- In the range of 0.01 to 0.6 μm roughness heights, splash is more likely to occur for low surface roughness.
- A surface roughness of 0.158 μm is enough to suppress splash for all the liquids tested.
- The tested commercial LFMs deposits well for a wide range of surface and jet speeds on surfaces with roughness levels similar to typical railhead roughness. However, splash may happen on very smooth railheads.
- On the surface with a mirror finish, both liquid jet speed and surface moving speed are salient to the occurrence of splash
- Increasing liquid viscosity helps to increase splash/deposition threshold for both Newtonian and non-Newtonian liquids on the mirror finish surface

5.2 Conclusions for jet and lamella shape and dimensions

An experimental investigation into the effects of fluid properties, liquid jet speed, liquid jet diameter and surface moving speed on lamella and jet shape and dimensions was carried out. A variety of liquid viscosities, elasticities, surface speeds, jet speeds and diameters were studied. The interaction between the impinging jet and the moving surface and the resultant lamella was observed through high speed imaging. The key findings of this study are:

- Lamella spread radius and width decreases with increasing surface speed and decreasing jet volumetric flow rate
- Lamella spread width to radius ratio is almost constant for all the cases tested, indicating a nearly constant lamella shape under all conditions.
- Average lamella thickness is proportional to square root of liquid kinematic viscosity, square root of liquid jet diameter and inversely proportional to square root of surface moving speed. This behavior is explained by reference to some simple theory.
- Average lamella thickness is not a function of liquid jet volumetric flow rate.
- For Newtonian liquids, lamella shape and dimensions can be predicted with knowledge of jet speed, diameter, liquid kinematic viscosity and surface speed using Equation 3-8.
- For the tested non-Newtonian liquids, three types of non-Newtonian behaviours were observed at high surface speed and low jet speed: jet necking, jet bending and jet stretching.

5.3 Recommendations for future work

To further advance the understanding of liquid jet impingement on a moving surface, investigation into the following areas should be considered:

- Effect of lamella geometry on splash behaviour.
- Lamella rim thickness distribution.
- More detailed study of splash/deposition threshold and the associated affecting factors on the mirror finish surface.
- Effect of liquid properties on the non-Newtonian behaviours: jet necking, bending and stretching
- In this study, test conditions are restricted in the current industrial application range (30~80 psig nozzle back pressure, 5~70 m/s surface speed). Broader test range may become necessary for future application.
- It is believed that liquid-air surface tension should have minimal impact on the lamella geometry, but this can be readily tested.

Bibliography

[1] Railway Association of Canada 2013, 2013 Rail Trends. Available from: The Railway Association of Canada. [July 2013].

[2] Y. Suda, T. Iwasa, H. Komine, T. Fuji, K. Matsumoto, N. Ubukata, T. Nakai, M.Tanimoto, Y. Kishimoto, The basic study on friction control between wheel and rail (experiments by test machine and scale model vehicle), in: Proceedings of the 6th International Conference on Contact Mechanics and Wear of Rail/Wheel Systems (CM2003), Gothenburg, Sweden. vol. II, 2003, pp. 343–348.

[3] Cotter, J., Eadie, D.T., Elvidge, D., Hooper, N., Robert, J., Makowsky, T., and Liu, Y., 2005. Top of Rail Friction Control: Reductions in Fuel and Greenhouse Gas Emissions. In: Proc. of the 2005 Conference of the International Heavy Haul Association (Rio de Janeiro), pp. 327-334.

[4] Eadie, D.T., Bovey, E., and Kalousek, J. (2002), The role of friction control in effective management of the wheel/rail interface, Railway Technical Conference, November 2002.

[5] Vuong, T. T., Meehan, P. A., Eadie, D. T., Oldknow, K., Elvidge, D., Bellette, P. A., & Daniel, W. J. (2011). Investigation of a transitional wear model for wear and wear-type rail corrugation prediction. Wear, 271(1), 287-298.

[6] Stock, R., Eadie, D. T., Elvidge, D., & Oldknow, K. (2011). Influencing rolling contact fatigue through top of rail friction modifier application–A full scale wheel–rail test rig study. Wear, 271(1), 134-142.

[7] Eadie, D. T., & Santoro, M. (2006). Top-of-rail friction control for curve noise mitigation and corrugation rate reduction. Journal of Sound and Vibration, 293(3), 747-757.

[8] MIWA, M., & MIZUNO, M. (2014). Modeling an Optimal Track Maintenance Schedule in Consideration of Train Derailment Risk. Quarterly Report of RTRI, 55(1), 51-59.

[9] Jun, X., & Qingyuan, Z. (2005). A study on mechanical mechanism of train derailment and preventive measures for derailment. Vehicle system dynamics: International Journal of Vehicle Mechanics and Mobility, 43(2), 121-147.

[10] M. Tomeoka, N. Kabe, M. Tanimoto, E. Miyauchi, M. Nakata, Friction control between wheel and rail by means of on-board lubrication, Wear 253 (2002) 124–129.

[11] Suda, Y., Iwasa, T., Komine, H., Tomeoka, M., Nakazawa, H., Matsumoto, K., ... & Kishimoto, Y. (2005). Development of onboard friction control. Wear, 258(7), 1109-1114.

[12] Lu, X., Cotter, J., & Eadie, D. T. (2005). Laboratory study of the tribological properties of friction modifier thin films for friction control at the wheel/rail interface. Wear, 259(7), 1262-1269.

[13] Watson, E. J. (1964). The radial spread of a liquid jet over a horizontal plane. Journal of Fluid Mechanics, 20(03), 481-499.

[14] Bohr, T., Putkaradze, V., & Watanabe, S. (1997). Averaging theory for the structure of hydraulic jumps and separation in laminar free-surface flows. Physical review letters, 79(6), 1038.

[15] Nóbrega, J. M., Carneiro, O. S., Pinho, F. T., Paulo, G. S., Tomé, M. F., Castelo, A., & Cuminato, J. A. (2007). The phenomenon of jet buckling: experimental results and numerical predictions. In The Polymer Processing Society 23rd Annual Meeting.(a)(b) t.

[16] Ribe, N. M. (2004). Coiling of viscous jets. Proceedings of the Royal Society of London. Series A: Mathematical, Physical and Engineering Sciences, 460(2051), 3223-3239.

[17] Cruickshank, J. O., & Munson, B. R. (1981). Viscous fluid buckling of plane and axisymmetric jets. Journal of Fluid Mechanics, 113, 221-239.

[18] Chiu-Webster, S., & Lister, J. R. (2006). The fall of a viscous thread onto a moving surface: a 'fluid-mechanical sewing machine'. Journal of Fluid Mechanics, 569, 89-111.

[19] Hlod, A., Aarts, A. C. T., Van De Ven, A. A. F., & Peletier, M. A. (2007). Mathematical model of falling of a viscous jet onto a moving surface. European Journal of Applied Mathematics, 18(06), 659-677.

[20] Gradeck, M., Kouachi, A., Dani, A., Arnoult, D., & Borean, J. L. (2006). Experimental and numerical study of the hydraulic jump of an impinging jet on a moving surface. Experimental thermal and fluid science, 30(3), 193-201.

[21] Fujimoto, H., Suzuki, Y., Hama, T., & Takuda, H. (2011). Flow Characteristics of Circular Liquid Jet Impinging on a Moving Surface Covered with a Water Film. ISIJ international, 51(9), 1497-1505.

[22] Keshavarz, B., Green, S. I., Davy, M. H., & Eadie, D. T. (2011). Newtonian liquid jet impaction on a high-speed moving surface. International Journal of Heat and Fluid Flow, 32(6), 1216-1225.

[23] KUMAR, P. (2011). Liquid Jet Interaction with a Moving Surface, (M.A.Sc. Thesis, UBC).

[24] Moulson, J. B. T. (2012). An experimental study of liquid jet impingement on a moving surface: the effects of surrounding air pressure and fluid properties, (M.A.Sc. Thesis, UBC).

[25] Keshavarz, B. (2011). Newtonian and elastic liquid jet interaction with a moving surface, (M.A.Sc. Thesis, UBC).

[26] Sterling, G. E. G. (2012). An experimental study on jet impingement on a very high speed moving surface, (M.A.Sc. Thesis, UBC).

[27] Moulson, J. B. T., & Green, S. I. (2013). Effect of ambient air on liquid jet impingement on a moving substrate. Physics of Fluids (1994-present), 25(10), 102106.

[28] Takamura, K., Fischer, H., & Morrow, N. R. (2012). Physical properties of aqueous glycerol solutions. Journal of Petroleum Science and Engineering, 98, 50-60.

[29] Dontula, P., Macosko, C. W., & Scriven, L. E. (1998). Model elastic liquids with water‐soluble polymers. AIChE journal, 44(6), 1247-1255.

[30] Bailey, F. E., & Callard, R. W. (1959). Some properties of poly (ethylene oxide) in aqueous solution. Journal of applied polymer science, 1(1), 56-62.

[31] Blandamer, M. J., Fox, M. F., Powell, E., & Stafford, J. W. (1969). A viscometric study of poly (ethylene oxide) in t‐butyl alcohol/water mixtures. Die Makromolekulare Chemie, 124(1), 222-231.

[32] Paul J. Flory. (1953). Principles of polymer chemistry. Cornell University Press: New York.

[33] Bueche, F. (1960). Mechanical degradation of high polymers. Journal of Applied Polymer Science, 4(10), 101-106.

[34] Glycerine Producers' Association. (1963). Physical properties of glycerine and its solutions. Glycerine Producers' Association.

[35] Mulligan, Q. (2014). M.A.Sc. Thesis (to appear), UBC.

[36] Hardy, A. E. J., & Jones, R. R. K. (2004). Rail and wheel roughness-implications for noise mapping based on the Calculation of Railway Noise procedure. AEA Technology Rail, 1, 46-52.

[37] Cordier, J. F., & Fodiman, P. (2000). Experimental characterization of wheel and rail surface roughness. Journal of Sound and Vibration, 231(3), 667-672.

[38] Rodd, L. E., Scott, T. P., Boger, D. V., Cooper-White, J. J., & McKinley, G. H. (2005). The inertio-elastic planar entry flow of low-viscosity elastic fluids in micro-fabricated geometries. Journal of Non-Newtonian Fluid Mechanics, 129(1), 1-22.

[39] Chiu-Webster, S., & Lister, J.R. (2006). The falling of a viscous thread onto a moving surface: a 'fluid-mechanical sewing machine'. Journal of Fluid Mechanics, 569, 89-111.

[40] Buckingham, E. (1914). On physically similar systems; illustrations of the use of dimensional equations. Physical Review, 4(4), 345-376.

[41] Middleman, S. (1995). Modeling axisymmetric flows: dynamics of films, jets, and drops. Academic Press.